JOURNAL OF GEOPHYSICAL RESEARCH, VOL. 114, D00A24, doi:10.1029/2008JD009946, 2009

Click Here for Full Article

Comparisons of global cloud ice from MLS, CloudSat, and correlative data sets

D. L. Wu,[1] R. T. Austin,[2] M. Deng,[3] S. L. Durden,[1] A. J. Heymsfield,[4] J. H. Jiang,[1] A. Lambert,[1] J.-L. Li,[1] N. J. Livesey,[1] G. M. McFarquhar,[5] J. V. Pittman,[6] G. L. Stephens,[2] S. Tanelli,[1] D. G. Vane,[1] and D. E. Waliser[1]

Received 9 February 2008; revised 10 November 2008; accepted 30 December 2008; published 18 April 2009.

[1] Aura Microwave Limb Sounder (MLS) version 2.2 (V2.2) and CloudSat R04 (release 4) ice water content (IWC) and partial-column ice water path (pIWP) measurements are analyzed and compared to other correlative data sets. The MLS IWC, representing an average over $\sim 300 \times 7 \times 4$ km^3 volume, is retrieved at 215–268 hPa with precision varying between 0.06 and 1 mg/m^3. The MLS pIWP products, representing the partial columns over $\sim 100 \times 7$ km^2 area with the bottom at $\sim$8, $\sim$6, and $\sim$11 km for 115, 240, and 640 GHz, have estimated precisions of 5, 1.5, and 0.8 g/m^2, respectively. CloudSat, on the other hand, shows a minimum detectable sensitivity of -31 dBZ in the reflectivity measurement at 94 GHz. CloudSat IWC is an average over $\sim 1.8 \times 1.4 \times 0.5$ km^3 volume, and its precision varies from 0.4 mg/m^3 at 8 km to 1.6 mg/m^3 at 12 km. The estimated single-profile precision for CloudSat IWP is $\sim$9 g/m^2. However, these measurements are associated with relatively large systematic error, mostly due to uncertainties in the retrieval assumptions about microphysics, which lead to relatively poor accuracy compared to measurement precision. To characterize systematic differences among various observations and those derived from models, we employ the normalized probability density function (pdf) in the comparisons. CloudSat IWC shows generally consistent slopes of pdf distribution with in situ observations, particularly at $\sim$12 km where the in situ data come mostly from long-leg flights. Despite similar IWC morphology found between MLS and CloudSat observations, CloudSat R04 IWC retrieval is higher compared to MLS, especially at 14–17 km where the MLS technique is not limited by sensitivity saturation. The MLS and CloudSat IWC pdf's agree well in the overlapped sensitivity range with relative difference <50%, but the difference appears to increase with IWC. MLS and CloudSat cloud ice measurements are compared with other data sets in terms of monthly map and pdf. Comparisons with European Center for Medium range Weather Forecasting (ECMWF) analyses show that grid box averages of monthly ECMWF IWC are much smaller (by $\sim 5\times$ and $\sim 20\times$) than the same MLS and CloudSat averages. Comparisons of pIWP data from CloudSat and passive sensors reveal large uncertainties associated with passive techniques, such as penetration depth and sensitivity limitation. In particular, retrievals from Moderate Resolution Imaging Spectroradiometer (MODIS) and Advanced Microwave Sounding Unit-B (AMSU-B) differ largely in IWP pdf from the CloudSat R04 retrieval, showing CloudSat values generally lower (by $\sim 5\times$ and $\sim 8\times$, respectively) at IWP = 10–500 g/m^2 but higher at IWP > 500 g/m^2.

Citation: Wu, D. L., et al. (2009), Comparisons of global cloud ice from MLS, CloudSat, and correlative data sets, *J. Geophys. Res.*, *114*, D00A24, doi:10.1029/2008JD009946.

[1]Jet Propulsion Laboratory, California Institute of Technology, Pasadena, California, USA.
[2]Department of Atmospheric Science, Colorado State University, Fort Collins, Colorado, USA.
[3]Department of Atmospheric Science, University of Wyoming, Laramie, Wyoming, USA.
[4]National Center for Atmospheric Research, Boulder, Colorado, USA.
[5]Department of Atmospheric Sciences, University of Illinois at Urbana-Champaign, Urbana, Illinois, USA.
[6]NASA Marshall Space Flight Center, Huntsville, Alabama, USA.

Copyright 2009 by the American Geophysical Union.
0148-0227/09/2008JD009946$09.00

1. Introduction

[2] Clouds are the major source of uncertainty in understanding and predicting Earth's climate variability and change [*Houghton et al.*, 2001; *Randall et al.*, 2007]. The amount of cloud ice in the troposphere, which has a critical impact on atmospheric radiation/energy balance, differs by several fold among the best climate models [*Li et al.*, 2005]. This leads to large uncertainties in the models to determine atmospheric radiation, circulation, and other variables or processes. For example, a 1 mg/m^3 error in cloud ice water content (IWC), equivalent to 10 ppmv error in upper tropospheric water vapor, could significantly alter greenhouse effects in the climate model. Water plays a key role in regulating the Earth's climate and weather systems through interchanges between its gas and condensed phases throughout the troposphere. These interchanges further complicate cloud roles in Earth's climate system and cloud feedbacks must be understood as a height-dependent process.

[3] Difficulties of measuring cloud ice with remote sensing arise from cloud variability and microphysics, which are so large and complicated that no single instrument, single technique, or single platform can measure them all [*Stephens and Kummerow*, 2007]. One of the difficulties with many satellite sensors is the inability of penetrating thick-and-dense clouds. For example, nadir infrared, visible, and UV techniques are limited to thin or the topmost layer of clouds. Even for the clouds penetrated by sensors, it remains challenging to accurately retrieve IWC ice water path (IWP) because of uncertainties associated with cloud microphysics, such as particle size distribution (PSD).

[4] Passive millimeter and submillimeter-wave techniques can penetrate deeper into clouds than infrared/visible techniques, and the cloud-induced microwave radiances are more direct measurements of IWC and IWP through interacting with most of ice scattering in the Rayleigh-Mie region [*Evans et al.*, 1998; *Weng and Grody*, 2000; *Hong et al.*, 2005; *Wu et al.*, 2005; *Eriksson et al.*, 2007]. Measurements from nadir-viewing instruments like Advanced Microwave Sounding Unit-B (AMSU-B) provide a broach swath and global coverage of cloud IWP on a twice-daily basis [*Zhao and Weng*, 2002]. A few additional slices of partial IWP column can be retrieved from spectral channels with different water vapor absorption [*Hong et al.*, 2005]. The Microwave Limb Sounder (MLS) instruments can measure IWC near the tropopause using high-frequency limb radiometry [*Wu et al.*, 2005; *Waters et al.*, 2006; *Wu et al.*, 2006]. Although this limb instrument does not have swath coverage, it provides a slightly better vertical resolution than nadir passive sounders by slicing cloud ice layers from the top of the troposphere. The MLS on NASA's Aura satellite consists of seven radiometers at frequencies near 118, 190, 240, 640 GHz, and 2.5 THz, and flies in formation with Cloud Profiling Radar (CPR) of CloudSat [*Stephens et al.*, 2002] as part of the NASA A-Train constellation. The synergy of passive-active sensors makes a great leap forward in satellite cloud observations, producing unprecedented ensembles of clouds that are measured closely space and time at multiple frequencies. These cloud data, although from a snapshot of fast cloud processes, contain valuable statistical information that can be utilized collectively to reduce uncertainties about microphysics and cloud ice retrievals. During normal operation, the Aura MLS (since August 2004) and CloudSat (since June 2006) have a twice-daily sampling from a sun-synchronous orbit. Joining with other instruments such as Cloud-Aerosol Lidar and Infrared Pathfinder Satellite Observations (CALIPSO) lidar, Atmospheric Infrared Sounder (AIRS), and Moderate Resolution Imaging Spectroradiometer (MODIS), the MLS and CloudSat instruments greatly extend A-Train cloud sensitivities by measuring hydrologically and radiatively important clouds in Earth's climate and weather systems.

[5] The MLS IWC retrieval, limited to 261–283 hPa, is based on a 240 GHz technique, and an initial validation of this product can be found in the work of *Wu et al.* [2008]. This paper extends the previous study to include MLS IWP retrievals from 115, 240 and 640 GHz, and compares MLS IWC and IWP morphologies and statistics with other satellite observations as well as with prognostic products from global assimilation systems. The aim of this study is to quantify, on a global basis, differences and limitations of various cloud ice observations, including MLS, CloudSat, MODIS, Atmospheric Radiation Measurement Program Tropical West Pacific (ARM TWP), Advanced Microwave Sounding Unit-B (AMSU-B), and in situ data. This study also aims to characterize differences between the observations and the diagnostic cloud ice products from global analysis systems, such as European Center for Medium range Weather Forecasting (ECMWF) and Goddard Earth Observing System Model, Version 5.1 (GEOS-5.1). Because of large spatiotemporal cloud variability and difficulties in obtaining coincident-and-collocated measurements, we choose to compare IWC and IWP statistics in terms of normalized probability density function (pdf). The pdf method does not rely on measurement coincidence and preserve key statistical properties of cloud data (Appendix A). From large ensembles of the A-Train data, we can develop reliable statistics to characterize measurement noise, bias, and sensitivity for various sensors. Depending on the measurement volume of individual samples, the pdf of IWC and IWP can be affected by cloud inhomogeneity. Thus, we always average high-resolution data spatially to match the volume of low-resolution data (e.g., MLS in many cases). The paper is organized to describe Aura MLS, correlative, and CloudSat measurements in sections 2–4, followed by the comparative study in section 5. Conclusions and future work are given in section 6.

2. MLS Data

2.1. Aura MLS Experiment

[6] Aura MLS is a passive limb instrument with seven radiometers at frequencies near 118 (H,V), 190(V), 240(H), 640(H) GHz and 2.5 (H,V) THz, of which the 118 GHz and 2.5 THz receivers measure radiances of both horizontal (H) and vertical (V) polarizations. All the MLS radiometers are sensitive to cloud-induced radiance changes at tangent heights < ~18 km [*Waters et al.*, 2006; *Wu et al.*, 2006]. All MLS radiometers except for the 118 GHz are double-sideband receivers, meaning that the measured radiance is a sum of radiation from two different frequency sidebands. The Aura MLS views forward in the satellite flying direction, and its (vertical, cross-track) field-of-view (FOV)

Table 1. Model Coefficients for the V2.2 T_{cir}-IWC Relations[a]

Ptan (hPa)	Retrieval Coefficient T_{cir0} (K)	Retrieval Coefficient α (mg/m^3)	Resolution[b] $H_{\parallel} \times H_{\perp} \times V$ (km^3)	Typical Precision[c] (mg/m^3)
83	100	40	200 × 7 × 5	0.06
100	100	40	200 × 7 × 5	0.07
121	100	43	250 × 7 × 4	0.1
147	90	55	300 × 7 × 4	0.2
177	80	69	300 × 7 × 4	0.3–0.6
215	70	70	300 × 7 × 4	0.6–1.3

[a]Adapted from *Wu et al.* [2008].
[b]$H_{\parallel}$, $H_{\perp}$ and V denote, respectively, the along-track, cross-track and vertical extent of the atmospheric volume sampled by an individual MLS measurement.
[c]These are typical 1σ precisions of single ice water content (IWC) measurements where the better values are for the extratropics and the poorer values for the tropics.

widths are (5.8, 12), (4.2, 8.4), (3.2, 6.4), (1.4, 2.9), and (2.1, 2.1) km for 118, 190, 240, 640 GHz and 2.5 THz, respectively.

[7] Launched in July 2004, the Aura satellite is in a sun-synchronous (~1340 ascending crossing time) orbit of 98° inclination at 705 km altitude. The MLS limb scans, covering latitudes between 82°S and 82°N, are synchronized to the orbital period to produce 240 limb scans per orbit during normal operation. Aura MLS scans continuously in tangent height (h_t) from the surface to ~92 km within 24.7s with an data integration time of 1/6 second for each limb measurement [*Waters et al.*, 2006]. A MLS GHz scan has 40–50 limb measurements dedicated to the troposphere with a sampling resolution of 300 m in tangent height [*Jarnot et al.*, 2006]. Only these low-h_t measurements are useful for cloud observations.

2.2. MLS Cloud Ice Retrievals

[8] The MLS cloud ice is retrieved from cloud-induced radiance (T_{cir}) in a window channel. T_{cir} is defined as the difference between the measured radiance and a modeled background for clear sky. T_{cir} uncertainty is dominated by error of the modeled clear-sky radiance. The background radiance of the window channels is typically ~20 K for 240 GHz at 100 hPa tangent pressure with precision of <0.5 K. At high tangent heights where the clear-sky background is relatively low (< ~100 K), T_{cir} is positive because the radiance from cloud scattering and emission is usually higher than the background. At low tangent heights where the clear-sky background is ~250 K, T_{cir} is negative because the radiance from cloud scattering is lower than the background and blocks the upwelling radiances. Clouds lack contrast from the clear-sky background at the intermediate tangent heights where uncertainties of the modeled radiance are also high (5–10 K), which makes clouds at this tangent height range difficult to detect.

[9] The MLS IWC data used in this study is the Version 2.2 (V2.2) retrieval, which is described by *Wu et al.* [2006, 2008]. This IWC product is retrieved from the 240 GHz T_{cir} measurements at 261–283 hPa, using modeled T_{cir}-IWC relations to convert T_{cir} to IWC. MLS IWP products used in this study are several independent retrievals using radiances from window channels near 115, 240 and 640 GHz at the bottom of each scan. These IWP retrievals represent a partial column of IWP (or pIWP) with a bottom height around 8, 6, and 11 km, for 115, 240 and 640 GHz, respectively. Like the IWC retrieval, pIWP is retrieved from a low-tangent-height T_{cir}. This retrieval first derives *h*IWP (the pIWP along the MLS LOS at that tangent height) from T_{cir} using modeled T_{cir}-*h*IWP relations. Then, *h*IWP is converted to pIWP (an IWP with respect to nadir) through a geometric relation. In the IWC and *h*IWP retrievals, the modeled T_{cir}-IWC and T_{cir}-*h*IWP relations are approximated by a nonlinear function

$$T_{cir} = T_{cir0}(1 - e^{-w/\alpha}) \quad (1)$$

where w is either IWC or *h*IWP, and coefficients T_{cir0} and α are given in Tables 1 and 2 for the IWC and *h*IWP, respectively. The T_{cir}-IWC or T_{cir}-*h*IWP relations were modeled by assuming a particle size distribution (PSD) [*McFarquhar and Heymsfield*, 1997] and homogeneously layered clouds for a tropical atmosphere.

[10] MLS V2.2 IWC data were validated by *Wu et al.* [2008] and compared to the CloudSat R03 IWC retrieval for July 2006 and January 2007. MLS IWC measurements should be interpreted as an ensemble average over the large volume near MLS tangent point (see Table 1). The V2.2 IWC uncertainty is dominated by cloud inhomogeneity and PSD errors. Because the inhomogeneity-induced uncertainties are mostly random, they can be reduced through averaging. However, inhomogeneity-induced scaling error, varying from −70% to +80%, and PSD-induced systematic error (as high as 100–200%) cannot be reduced by averaging [*Wu et al.*, 2008].

[11] The standard MLS V2.2 IWP, or $pIWP_{>6km}$, is retrieved from the 240 GHz T_{cir} at the ~650 hPa tangent pressure where the radiance is mostly saturated and less sensitive to the surface emission because of strong atmospheric attenuation. The retrieved $pIWP_{>6km}$ is reported at the tangent point location, but the actual measurement location (where the saturation occurs) is ~300 km (or ~2 nominal MLS profiles) away from the tangent point toward MLS. In addition to the 240 GHz measurement, MLS 115, 190 and 640 GHz radiometers also measure pIWP independently but for different partial columns. As shown in Figure 1, MLS T_{cir} from the four radiometers have different penetration depths, which depend on water vapor and dry continuum absorptions as well as on cloud extinction itself. To estimate the bottom height where these radiometers can penetrate, we compute the transmission function for these frequencies assuming a cloud ice column of 30 g/m^2. We then determine the contribution function by

Table 2. Estimated MLS IWP Partial Column, Precision, and Sensitivity Range[a]

MLS Radiometer	Retrieval Coefficient T_{cir0} (K)	Retrieval Coefficient α (kg/m^2)	Bottom Height (km)	Resolution $H_{\parallel} \times H_{\perp}$ (km)	Estimated Precision (g/m^2)
R1 (115 GHz)	−59	19	~8	120 × 12	5
R2 (190 GHz)	−160	9.5	~7	80 × 8	2
R3 (240 GHz)	−180	5.2	~6	60 × 6	1.5
R4 (640 GHz)	−150	1.6	~11	30 × 3	0.8

[a]MLS, Microwave Limb Sounder; IWP, ice water path.

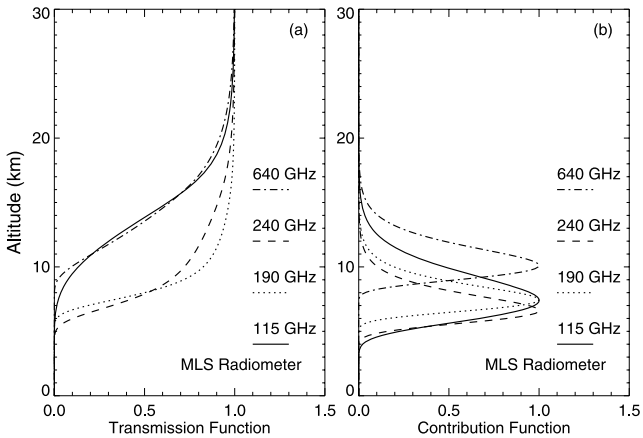

Figure 1. (a) Calculated Microwave Limb Sounder (MLS) transmission functions as a function of altitude at the window channel of the 115, 190, 240, and 640 GHz radiometers. (b) Contribution functions to MLS ice water path (IWP) estimated by assuming the ice water content (IWC) vertical distribution in form of $e^{-z/1\mathrm{km}}$. The bottom of pIWP is defined as the altitude at which the contribution function peaks, and they are approximately 8, 7, 6, and 11 km for 115, 190, 240, and 640 GHz, respectively.

weighting the transmission function with an exponential IWC profile, i.e., $IWC \propto e^{-z/H0}$, where H_0 is the mean scale height of IWC profiles. Observations from in situ measurements [*Heymsfield and Donner*, 1990; *McFarquhar and Heymsfield*, 1996] suggest that H_0 is ~2 km in the tropical upper troposphere but becomes steeper (~1 km) near the tropopause. We define the "bottom" of pIWP as the peak altitude of the contribution in Figure 1b, which are approximately 8, 8, 6, and 11 km for 115, 190, 240 and 640 GHz. The "bottom" of pIWP is a rough estimate of the lower cutoff of the partial column, and the number can alter significantly with cloud ice amount in the column. Hereinafter, we also denote these pIWP retrievals as $IWP_{>8km}$, $IWP_{>8km}$, $IWP_{>6km}$, and $IWP_{>11km}$, respectively.

2.3. Spatial Resolution

[12] The MLS long limb path has both advantages and disadvantages in sensing upper tropospheric cloud ice. The long path helps to detect thin cirrus layers with low ice mass and covering an extensive area, which would produce a weak signal from nadir-viewing sensors. MLS narrow vertical FOV (3.2 km at 240 GHz) can effectively reduce surface and cloud contributions from altitudes below the pointing tangent height. On the other hand, the long limb path has poor horizontal resolution by smearing out cloud fields along the LOS, and require careful interpretation about the averaged cloud quantities. Because of the spatial smearing, MLS IWC measurements should be viewed as an ensemble average of cloud ice (Figure 2). The concept is particularly important when comparing MLS cloud ice measurements with other correlative data, and a spatial averaging must be considered to match each other's measurement volume for a fair comparison.

[13] Effects of MLS FOV smearing on cloud ice measurements depend on cloud horizontal and vertical inhomogeneity, but knowledge about inhomogeneous structures was limited priori to the launch of CloudSat. In the upper troposphere, statistics from in situ measurements suggest that the ensemble mean of cloud IWC tend to decrease with height exponentially [*McFarquhar and Heymsfield*, 1997]. This property leads to a simple, nearly linear relation between MLS T_{cir} and IWC, because the T_{cir}-IWC sensitivity peaks near the pointing tangent height where T_{cir} is measured [*Wu et al.*, 2005]. This is also a basis to form the MLS V2.2 IWC retrieval [*Wu et al.*, 2008]. As expected for the coarse horizontal resolution, cloud inhomogeneity may induce error when interpreting MLS IWC measurements. This error appears to be mostly random and can be averaged down in a monthly or seasonal map as studied by *Wu et al.* [2008]. To improve the IWC horizontal resolution, the MLS team is currently developing a tomographic retrieval, which uses information from adjacent scans (separated by ~165 km) to produce IWC profiles at a horizontal resolution of ~50 km. Compared to IWC, MLS IWP has a slightly better horizontal resolution (Table 2) because the measurement comes from a slant viewing angle (Figure 2).

2.4. MLS Monthly Maps

[14] Cloud ice mass and distribution have profound impacts on global atmospheric circulation and precipitation [*Ramanathan et al.*, 1989; *Hartmann and Larson*, 2002; *Stephens*, 2005]. Research in the past has been focused on effects of clouds on radiation and latent heating at the top or bottom of atmosphere, while the radiative and hydrological processes inside clouds are poorly constrained. The lack of observational constraint on cloud representation in climate models makes the cloud-climate feedback problem ill-posed, leading to low confidence on model predictability for future climate changes. The new global observations of cloud ice in the middle and upper troposphere begin to infuse additional constraints on the models, which allow

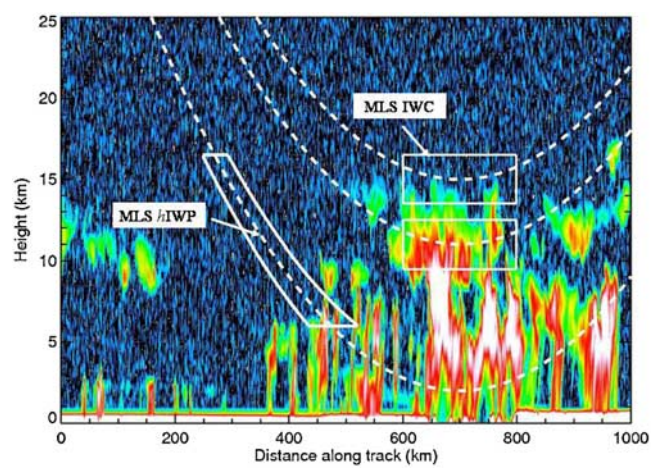

Figure 2. Diagram to illustrate the MLS smearing on the IWC measured by CloudSat. The dashed lines are the MLS tangential beams. At high tangent heights, the beams penetrate through the limb and become sensitive to a volume-averaged IWC, whereas at low tangent heights the MLS beams cannot penetrate through the limb because of strong gaseous absorption and become only sensitive to a partial column of IWP, namely, *h*IWP, with a shallow angle (~3°). Note that the actual volume of the *h*IWP locates at ~300 km away from the tangent point, or ~2 profiles toward MLS.

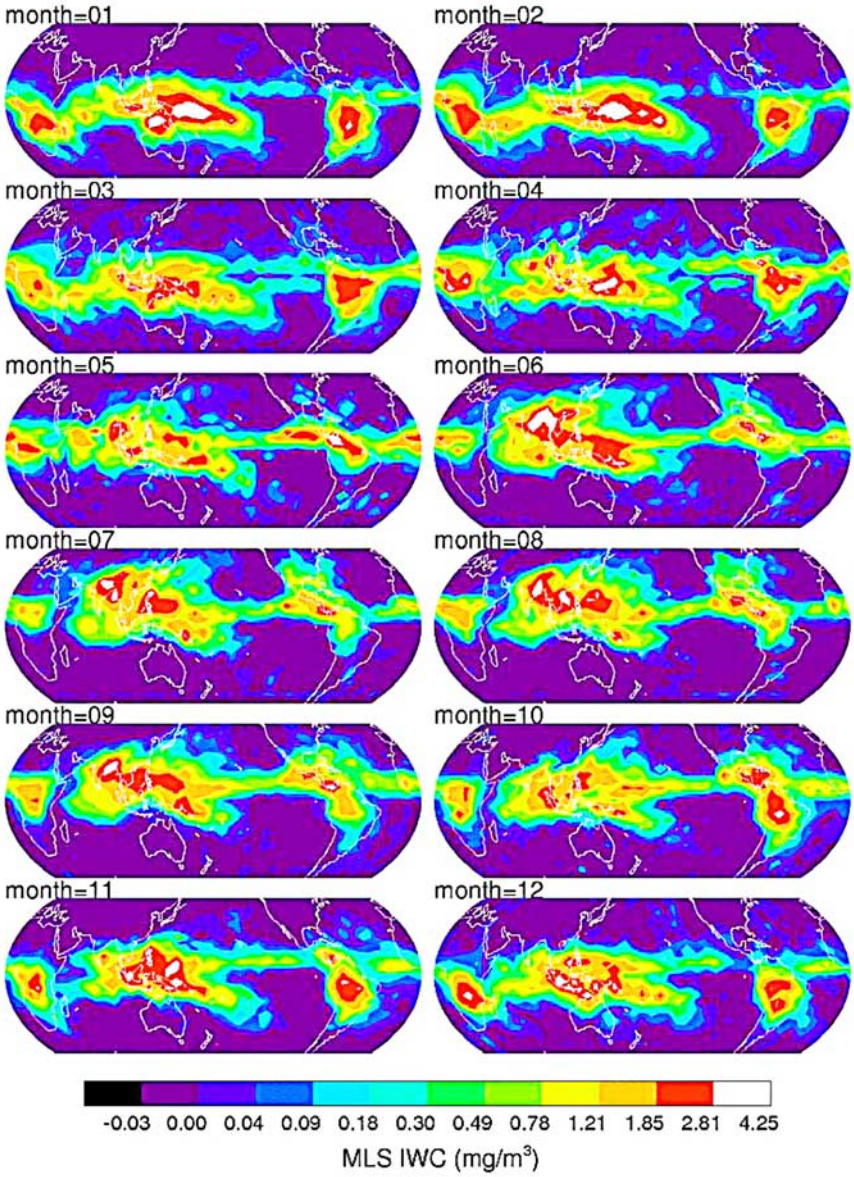

Figure 3. MLS V2.2 monthly mean IWC at 147 hPa for latitudes between 50°S and 50°N from 2004–2007. Both ascending and descending measurements are averaged into 4° × 8° latitude-longitude boxes, and the IWC value is an all-sky mean. The IWC data are screened on a daily basis, and the values with IWC < 3σ are zeroed.

modelers to diagnose and evaluate model physics, parameterization, and predictability under a new set of observed cloud statistics.

[15] Figures 3–4 show the monthly maps of MLS 147-hPa IWC and $IWP_{>6km}$ averaged for the period August 2004 to December 2007. The MLS IWC distributions in Figure 3 reflect the transition from an austral summer season when the main cloud ice features are associated with continental convection over Central Africa and South America, and intense convection over the western Pacific, to a boreal summer season dominated by the Asian and central American monsoons. These seasonal variations in MLS cloud ice reflect changes of large-scale dynamics and variability in regional weather and climate. For example, upper tropospheric cloud ice from the Asian monsoon occurs preferentially in the Bay of Bengal and the Western Pacific (in July–September).

[16] In the tropics, MLS IWC distribution correlates well with the intertropical convergence zone (ITCZ). Like in precipitation climatology, the ITCZ structures in MLS IWC oscillate with season about the equator but remain at a relatively stationary northern latitude over oceans. However, the IWC distribution in Figure 3 exhibits a large gradient between the eastern and western Pacific, and this gradient varies seasonally with very low cloud ice during December–February. In January–February, cloud ice lifted into the upper troposphere is substantial over the western Pacific warm pool (WPWP) where super convective clusters are often formed [*Houze et al.*, 2000]. In the meantime (January and February), cloud ice from the southern Pacific conver-

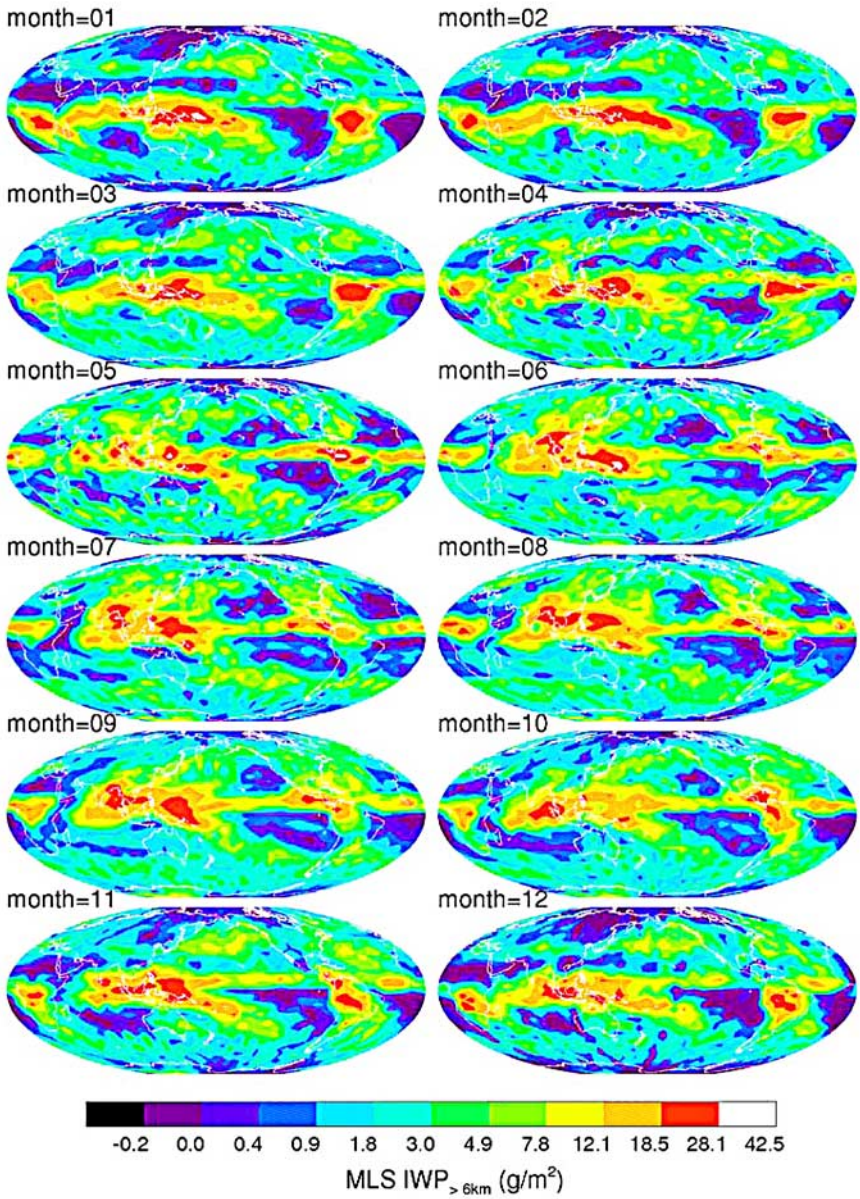

Figure 4. As in Figure 3 but for MLS V2.2 $IWP_{>6km}$ from 2004–2007. The maps are restricted to latitudes between 80°S and 80°N.

gence zone (SPCZ) strengthens to its annual maximum. Between May and September, the Asian monsoon brings up large IWC at latitudes between the equator and 40°N, affecting an area 4–5 times larger than the American monsoon. In October the 147-hPa IWC over the WPWP region exhibits a distribution pattern that resembles the Gill's solution in response to a large-scale tropical diabatic heating [*Gill*, 1980]. The Gill's solution generates an eastward propagating Kelvin wave and a westward propagating Rossby wave, and these wave patterns can be readily seen in weekly MLS IWC maps as well as in MLS relative humidity with respect to ice (RHi) maps. Impacts of the Madden-Julian Oscillation (MJO) on these wave patterns and IWC distribution over the upper tropospheric western Pacific are studies by *Schwartz et al.* [2008]. During July–October the $IWP_{>6km}$ enhancement between the eastern Pacific ITCZ and the SPCZ appears to be associated with midtropospheric cloud ice since it is not seen in the 147-hPa IWC maps.

[17] The two equatorial bands seen in MLS 147-hPa IWC during March and April over the eastern Pacific are a manifestation of the double ITCZ as reported previously in other satellite observations [*Waliser and Gautier*, 1993; *Lietzke et al.*, 2001; *Halpern and Hung*, 2001; *Liu and Xie*, 2002]. The double-ITCZ feature is more pronounced and clearly defined in the IWC maps than in $IWP_{>6km}$. Although it appears in MLS IWC maps at pressure levels between 261 and 121 hPa, the feature is not evident in the 100-hPa IWC map.

[18] Unlike the IWC, the $IWP_{>6km}$ exhibit cloud ice enhancements at midlatitudes and high latitudes (Figure 4), as a result of penetration into the midtroposphere. In the Northern Hemisphere, Pacific and Atlantic storms contribute mostly to the midtropospheric cloud ice over the oceans

during the period between October and January. In the Southern Hemisphere, storms bring up significant midtropospheric cloud ice between April and September. In the Tropics, the seasonal variation of $IWP_{>6km}$ is similar to that in the 147-hPa IWC, high in February–October and low in November–January. Note that the Gill's pattern in the October $IWP_{>6km}$ map is not as clear as in the 147-hPa IWC map because the $IWP_{>6km}$ quantity likely smear out Gill's solution that has a characteristic vertical structure.

3. Correlative Data

[19] Before the MLS-CloudSat comparisons, we introduce several cloud ice data needed in this study, which include those from in situ sensors, ground-based radars, passive satellite imagers, and model assimilations. The in situ aircraft data used in this study, which are generally considered as the best cloud ice measurements, represent a collection of Central Equatorial Pacific Experiment (CEPEX), NASA African Monsoon Multidisciplinary Analyses (NAMMA), and Cirrus Regional Study of Tropical Anvils and Cirrus Layers-Florida Area Cirrus Experiment (CRYSTAL-FACE), or CF. The primary motivation of using in situ data is to validate the slope of IWC pdf's at different altitudes. The ground-based radar data are from Atmospheric Radiation Measurement (ARM) Program tropical sites. IWP data from MODIS and AMSU-B provide 2-D images of cloud ice that can potentially be retrieved from Vis/IR and microwave techniques. Finally, global assimilation systems developed by ECMWF and Global Modeling and Assimilation Office (GMAO) have produced prognostic products for cloud ice from other analysis variables. A better understanding of the prognostic products is a key step toward integration of cloud ice dynamics into climate/weather systems.

3.1. CEPEX IWC

[20] CEPEX was conducted in the region of 20°S–2°N and 165°E–170°W during March–April 1993 with the campaign focus on cirrus outflows from deep convection. In situ measurements from CEPEX covered altitudes of ambient temperatures between −70°C and −20°C [*Heymsfield and McFarquhar*, 1996; *McFarquhar and Heymsfield*, 1997]. CEPEX IWC, mostly observed at ~11.5 km altitude (a cruising altitude) and ranging between 10^{-4} and 1 g/m^3, is derived from measured cloud microphysical properties. At the cruise altitude, the data were collected continuously over a long distance, in which clear and cloudy skies were sampled in a way very much like satellite observations. The data from long-leg flights are particularly useful for comparison to satellite observations because of the fair sampling for clear and cloudy conditions. The another cruise altitude in CEPEX was at ~7 km but with a much shorter duration or coverage than that from 11.5 km.

3.2. NAMMA IWC

[21] The NAMMA campaign was commenced in August 2006 off the coast of west Africa (10°N–20°N and 10–40°W) to study formation, evolution and impact of Saharan air layers on tropical hurricanes in the eastern and central Atlantic. The IWC data used here are direct measurements from the Counterflow Virtual Impactor (CVI) instrument. The cruise altitude is ~10 km, where more data were collected than other altitudes, but the data were biased toward mesoscale convective systems and sampled often over a short distance. NAMMA flights were designed to probe clouds at different altitudes through spiral sampling, and therefore, cloud statistics from the NAMMA campaign are likely skewed to convective cloud types.

3.3. CRYSTAL-FACE IWC

[22] The CRYSTAL-FACE campaign was conducted in July 2002 to study cirrus outflows in the subtropics. The IWC data used in this study were measured by the CVI instrument with uncertainty ranging from 11% at 0.2 g/m^3 to 23% at 0.01 g/m^3. The CVI measurements are saturated at ~ 1 g/m^3. Clouds were sampled mostly from ascending-descending flight paths that cover a height range between −25°C and −52°C. No flights were as long as in the CEPEX campaign with a constant cruising altitude.

3.4. ARM Cloud Radar Data

[23] The ARM cloud profiling radars provide long-term ground-based measurements in several sites that contain valuable statistics on cloud ice [*Clothiaux et al.*, 2001; *Mace et al.*, 2001]. In this study we use the compiled statistics based on hourly averaged IWP measurements from the ARM Tropical West Pacific (TWP) sites, namely Nauru (0.5°S, 167°E) and Manus (2°S, 147°E) Island, where the IWP is retrieved using the algorithm developed by *Deng and Mace* [2006]. The ARM 35 GHz radar was up for 90% of time at (65% useful) and 44% uptime at Manus in 2005. During the general operation mode, the radar has 90 m range resolution with coherent averaging. Although it is designed to achieve 70 dBZ dynamic range between −50 and +20 dBZ with different operational modes, the estimated minimum cloud sensitivity at and Manus sites is about −41 and −48 dBZ, respectively [*Clothiaux et al.*, 2001].

3.5. AMSU-B IWP

[24] The AMSU-B IWP is retrieved with the algorithm developed by *Weng and Grody* [2000] and *Zhao and Weng* [2002]. The algorithm retrieves IWP and effective diameter D_e simultaneously retrieved using cloud scattering signatures at 89 and 150 GHz. Thus, the AMSU-B IWP should have a sensitivity similar to MLS 115 GHz, except that the nadir sounder can penetrate slightly deeper in the atmosphere. AMSU-B has better horizontal resolution (15 km at nadir) and swath coverage (2300 km) than MLS. Similar to MLS, the AMSU-B algorithm first estimates the clear-sky radiances at 89 and 150 GHz using the retrieved atmospheric state from AMSU-A 23 and 31 GHz measurements, and then determines T_{cir} from the measured-modeled radiance difference. The derived T_{cir} are not used for IWP retrieval if the value is below a cloud detection threshold, and IWP is zeroed in these cases. The T_{cir}-IWP relation used in the IWP retrieval is modeled by *Zhao and Weng* [2002], assuming a modified gamma size distribution for ice particles.

3.6. MODIS IWP

[25] A MODIS instrument [*Salomonson et al.*, 1989; *Barnes et al.*, 1998] was flown on the Aqua satellite since May 2002, which has the same suborbital track as CloudSat

and MLS. It precedes CloudSat by approximately one minute and MLS by ~8 minutes. MODIS measures radiances between 0.4 and 14.2 μm over 36 spectral bands. At nadir, the horizontal resolution ranges from 250 m to 1 km depending on wavelength, and the instrument covers a swath 2330 km wide. In this study, we use Collection 5, daily, daytime, Level 3 data (MYD08_D3) on a 1° × 1° (longitude and latitude) grid box. In this study the MODIS measurements are analyzed at latitudes between 25°N and 25°S for the period between 7 July and 16 August 2006. IWP is derived from the *ice cloud optical thickness* and the *ice cloud effective radius* products, which are obtained from water-absorbing near-infrared bands (1.6, 2.1, and 3.7 μm) and nonabsorbing visible and near-infrared bands (0.65, 0.86, and 1.2 μm), using the following relation [*Stephens*, 1978]:

$$IWP = \frac{4\rho\tau r_e}{3Q_e} \tag{2}$$

where ρ = 0.93 g/cm^3 is the density of ice, τ is the optical thickness, r_e is the cloud effective radius, and $Q_e \sim 2$ is the extinction efficiency. Equation (2) assumes a vertically uniform effective radius and a constant cloud phase throughout the column, which is determined by the cloud top phase. This calculation and determination is performed with the Level 2 data. The Level 3 data are then reported either as histograms with predetermined IWP bin sizes or as average IWP values within each 1° × 1° grid box. In this study, we do not constrain our analysis to the MODIS predetermined IWP bin sizes. Instead, we use the average IWP value representative of each 1° × 1° grid box. The average IWP approach produces a pdf that is ~50% higher for IWP less than 10 g/m^2, within ±20% for IWP between 10 and 1000 g/m^2, and 80 to 100% lower for IWP greater than 1000 g/m^2 compared to the histogram IWP approach. The reduction in the frequency of the infrequent and extreme IWP events in the average IWP approach can be explained by the averaging effect on cloud inhomogeneity that takes place within the grid box. Despite these differences, the use of the average IWP approach in our multisensor IWP analysis does not change the conclusions of this study.

3.7. ECMWF T_L799L91 Analyses

[26] Most of the modern global analyses can produce a diagnostic product for cloud ice. Despite observation uncertainties and limitations, satellite cloud ice data have demonstrated their values for improving cloud parameterization in global numerical models [*Li et al.*, 2005]. Here we make brief comparisons of MLS and CloudSat IWC to the latest data from ECMWF Integrated Forecast System (IFS), T_L799L91 Cycle 30r1, which are output 6-hourly at 00, 06, 12 and 18Z for the same period 7 July to 16 August 2006. Cloudy-sky satellite observations are not assimilated in the ECMWF DAS [*Chevallier et al.*, 2004] but microwave information in rainy regions are utilized [*Bauer et al.*, 2002]. In other words, cloud properties in the analysis directly result from the analyzed temperature, humidity and velocity fields according to physics of the cloud scheme. Neither MLS nor CloudSat data are assimilated by the ECMWF DAS.

[27] The T_L799L91 model is the latest ECMWF DAS in assimilating atmospheric observations, and has been operational since February 2006. The horizontal resolution of T_L799 gives the highest resolved wave number at 50 km, improved from 78 km in T_L511. A better representation of world topography in the new system directly improves forecasts of weather phenomena as well as wave excitation influenced by orographic features. Vertically, the number of model layers is increased to 45–50 levels in the troposphere with a nearly doubled resolution near the tropopause, and 40–45 levels in the stratosphere and mesosphere with the top at ~80 km. Other improvements include a shortened (12 min) time step and an increased horizontal resolution (0.36°) in coupled ocean wave model.

3.8. GEOS-5.1 Analyses

[28] The Version 5.1 Goddard Earth Observing System (GEOS-5.1) data analysis is developed in the NASA GMAO, which has the same physics package as in its earlier version (GEOS-4) [*Bloom et al.*, 2005]. GEOS-5.1 adopts the 3D-Var approach to produce data assimilation every 6-hourly (00Z, 06Z, 12Z and 18Z) on 72 model levels from the surface to 0.01 hPa with a 0.5° × 0.67° latitude-longitude resolution. Like the ECMWF analysis, the GEOS-5.1 cloud ice is a diagnostic product, derived from temperature, moisture and other related atmospheric state quantities.

4. CloudSat Data

[29] Launched in April 2006, CloudSat is the first spaceborne 94-GHz cloud profiling radar (CPR) to measure vertical structures of cloud and precipitation [*Stephens et al.*, 2002; *Im et al.*, 2005]. Each CPR profile has a range resolution of ~500 m but the measurements are reported on an increment of ~240 m between the surface and ~28 km altitude. The effective dimensions of a single measurement are approximately 1.4 km cross-track and 1.8 km along-track with the along-track sampling at every 1.1 km. The 1.8 km along-track resolution results from convolution of the antenna beam width (1.4 km) and data integration smearing (1.1 km in distance). Since 16 August 2006, instead of pointing at the geodetic nadir, the CloudSat antenna beam was moved to an off-nadir (0.16° in the forward direction) position to reduce specular surface reflectance during normal operation. In the current A-Train configuration, Aura MLS and CloudSat measurements are separated by 7–8 min in time, but their measurement tracks are separated by ~200 km at low and midlatitudes. Thus, MLS and CloudSat measurements are not collocated for tropical clouds. Since May 2008, Aura has been moved closer to CloudSat and Aqua such that MLS footprints at the 10-km tangent height are now collocated with CloudSat/CALIPSO samples within ±5 km. Under this new A-Train configuration, the MLS observations will be able to compare with CloudSat, CALIPSO, and Aqua measurements on a point-by-point basis, of which the data will be analyzed in future studies.

[30] Radar reflectivity factor *Ze* is a fundamental cloud measurement from CPR, which can be derived from the ratio of received cloud backscattering power (P_r) over transmitted power (P_t). CloudSat's *Ze* is defined with

respect to liquid water [*Li and Durden*, 2006]. In the CloudSat R04 (release 4, algorithm version 5.1) data, the CPR *Ze* is set to zero by the 2B-GEOPROF algorithm when it is below a noise threshold [*Mace et al.*, 2007]. One of the objectives in this study is to evaluate CloudSat measurement error under different spatial averaging (see section 5). Truncated noise characteristics by the 2B-GEOPROF algorithm would lead to a biased evaluation on measurement uncertainty and minimum detection level of CloudSat measurements averaged for different volumes. Hence, as described in the following, we examined measurement noise more carefully and carried out a slightly different calculation for CloudSat *Ze* in this study.

[31] The received power (P'_r) contains noise power (P_n) and cloud backscattering power (P_r), i.e., $P'_r = P_r + P_n$. To derive CloudSat *Ze* ($Ze \propto P_r/P_t$), we need to first evaluate P_n, and then remove P_n from P_r. Because both surface and cloud thermal emissions can contribute to P_n, it is more accurate to determine P_n on a profile-by-profile basis, rather relying on measurements from adjacent profiles [*Tanelli et al.*, 2008]. In this study we estimate P_n from P'_r within each profile at the top 40 bins (corresponding to altitudes > ~18 km) where measurements are rarely contaminated by clouds. To ensure the quality of the background measurements, we exclude contaminated data in the 40 bins, which may sometimes come from aliased echoes generated beyond the maximum unambiguous range (e.g., because of multiple scattering in heavy precipitation cases, or the so-called mirror image), and sometimes from clouds with a rarely high top. The contaminated data are removed by discriminating spikes that are two standard deviations above/below the estimated mean of the 40 measurements. The screened data from the 40 range bins are then used to calculate the mean and standard deviation again. This screening and evaluation procedure is repeated for several (usually <4) times until the convergence is reached. If all of the 40 measurements are used for the P_n estimation, the estimated precision of P_n will be improved to $\sigma_n/\sqrt{40}$ or $0.16\sigma_n$, where σ_n is the single measurement precision of CPR at a single range bin. The final mean will be the estimated noise power $\hat{P}_n$, and cloud backscattering power P_r can be determined by $P'_r - \hat{P}_n$. For low signal-to-noise ratio the precision of P_r is dominated by the noise σ_n and the subtraction manipulation induces additional noise $\sigma_n/\sqrt{40}$ to σ_n for the resulting cloud reflected power. Hence, we obtain an estimated precision for single cloud power measurement, which is defined by $\sqrt{1 + 1/40}\sigma_n$, or $\sim 1.01\sigma_n$. As shown later, it corresponds to a value of −31 dBZ for tropical measurements if one uses the prelaunch calibration coefficients [*Li and Durden*, 2006].

[32] In the CloudSat R04 data, P_n is calculated similarly but using measurements from adjacent profiles, and CPR reflectivity is set to zero by the 2B-GEOPROF algorithm when it is below P_n [*Mace et al.*, 2007]. IWC is retrieved together with a width parameter that is used to characterize the lognormal size distribution for particle sizes. The radar-only IWC retrieval in R04 [*Austin et al.*, 2009], part of the CloudSat 2B-CWC-RO products, retrieves profiles of three particle size distribution parameters using in situ measurements as the *a priori* constraint. The width parameter and number concentration in an earlier release (R03) is independent of height, which was thought as a primary cause for the R03 retrieval being low against MLS at high altitudes [*Wu et al.*, 2008]. Both R03 and R04 retrievals zero IWC if ambient temperature is above 0°C and scale down IWC linearly for temperatures from −20°C to 0°C as the partition between ice and liquid water contents. A major improvement with the R04 retrieval is its better handling of intensive cloud cases where the R03 retrieval often failed [*Austin et al.*, 2009]. The failed cases are ~2% out of all measurements, which affect significantly the statistics of thick-and-dense clouds. The R04 algorithm is able to retrieve most of these cases and reduces the failure rate to <0.2%.

[33] In addition to the CloudSat algorithms [*Austin and Stephens*, 2001; *Benedetti et al.*, 2003; *Austin et al.*, 2009], other methods have been proposed to retrieve IWC from 94-GHz radar reflectivity, most of which use a direct *Ze*-IWC relation derived from ground or airborne observations [e.g., *Atlas et al.*, 1995; *Brown et al.*, 1995; *Aydin and Tang*, 1997; *Liu and Illingworth*, 2000; *Sassen et al.*, 2002; *Matrosov et al.*, 2002; *Heymsfield et al.*, 2005; *Hogan et al.*, 2006; *Protat et al.*, 2007; *Sayres et al.*, 2008]. These algorithms assume a log-linear relation between *Ze* and IWC, and characterize it with two empirical parameters that are either constant or as a function of temperature and *Ze* (Table 3). We selected two retrievals from the list to compare with the R04 IWC retrieval: namely, *Hogan et al.* [2006] (hereinafter H06) and *Sayres et al.* [2008] (hereinafter S08). However, we modified these *Ze*-IWC relations slightly to include noise propagation by allowing the retrieval of negative *Ze* values, which is shown in equation (3). The noise-included retrieval is achieved by converting the absolute value of *Ze* to IWC using the proposed *Ze*-IWC relation, and assigning the *Ze* sign back to the retrieved IWC after the conversion. Mathematically, it can be written as

$$IWC = \mathrm{sign}(Ze)a|Ze|^b \tag{3}$$

where IWC has unit of g/m^3, and empirical coefficients a and b can be found in Table 3. Note that radar reflectivity factor *Ze* (mm^6/m^3) in equation (3) is taken for its absolute value so that negative *Ze* is concerted to negative IWC. Preserving the full IWC statistics (by including negative retrieval values) is important when comparing averaged CloudSat IWC with other data sets. However, as shown later in Figure 5, the IWC statistics from the 2B-IWC-RO retrieval are incomplete, missing noise characteristics of the IWC measurement.

[34] Figure 5 shows the normalized pdf's of CPR reflectivity for $Ze > 0$ and the IWC retrievals from three algorithms (R04, H06, S08). The rising pdf at $Ze < -31$ dBZ in Figure 5a is a manifestation of the Gaussian noise from the measurement (Appendix A). The −31 dBZ standard deviation is the best fit to the rising pdf at small positive values as well as negative values (not shown). This estimated CloudSat minimum detectable sensitivity is about 6 dB better than the mission requirement of −26 dBZ for three consecutive beam averaging at the end of prime mission [*Im et al.*, 2005; *Tanelli et al.*, 2008]. The pdf's at $Ze > -31$ dBZ are dominated by cloud contributions, showing a log-linear distribution over a broad dynamic range between −31 and 15 dBZ. Cloud occurrence diminishes sharply at $Ze > 20$ dBZ in the upper troposphere although the CPR can measure a reflectivity up to 40 dBZ. As an interesting cloud property, the *Ze* pdf's all

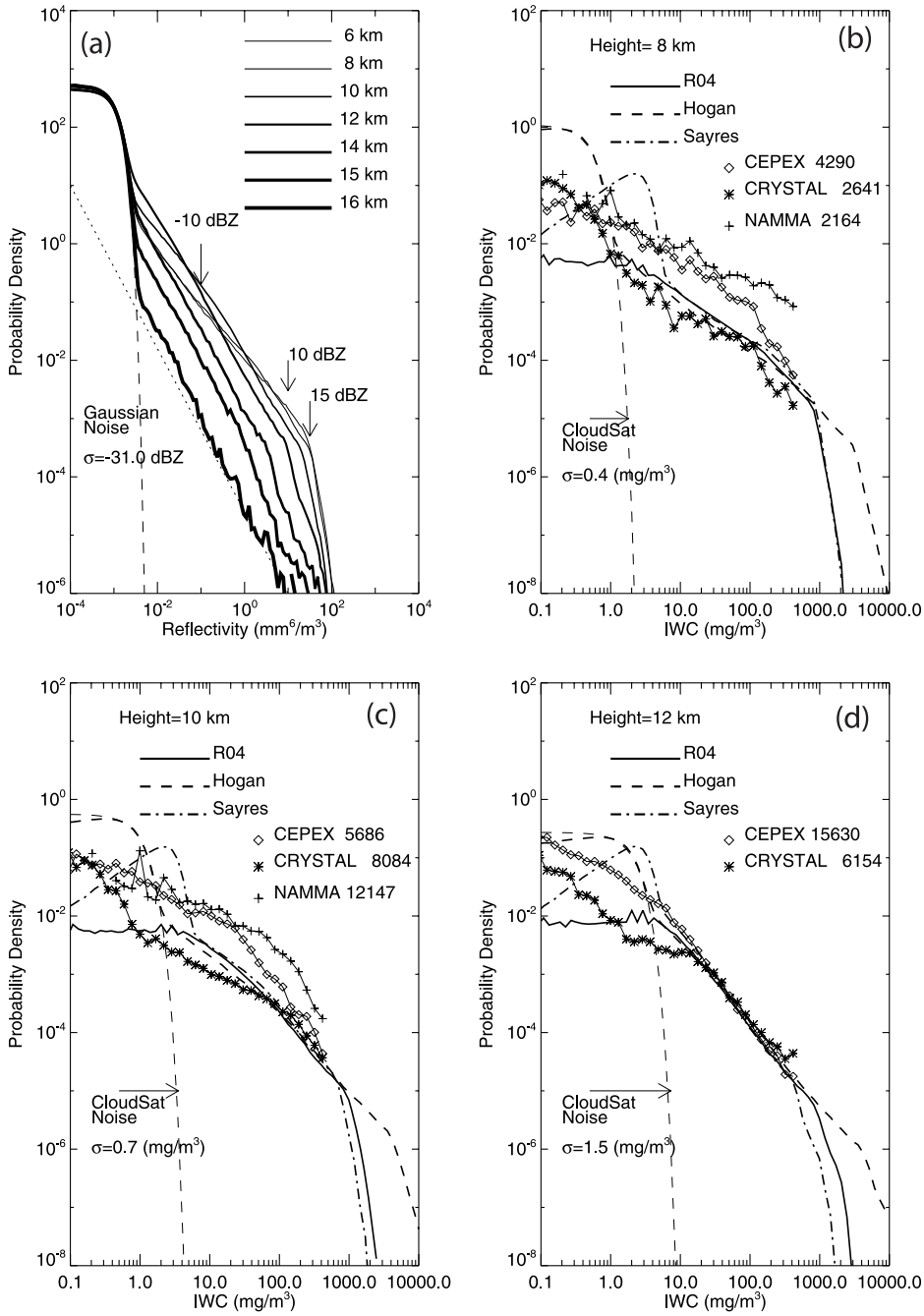

Figure 5. Normalized pdf's of CloudSat (a) reflectivity *Ze* and (b–d) IWC at 8, 10, and 12 km for 7 July to 16 August 2006 in a tropical bin (25°S–25°N). The rising pdf at small *Ze* is a manifestation of Gaussian noise with the standard deviation of −31 dBZ. The dotted line indicates the slope of pdf with Ze^{-1}, which appears to be universal at altitudes >12 km. CloudSat *Ze* pdf drops sharply at $Ze > 15$ dBZ at altitudes ≤10 km, indicating strong attenuation by clouds. The pdf's of negative *Ze* values are not shown since they are similar to the rising pdf at small positive values. The CloudSat IWC noise is estimated from the H06 method with the standard deviation shown, whereas the estimated error from the S08 method would be 2–5 times larger depending on altitude. The pdf of the R04 retrieval appears to be white at IWC < ∼4 mg/m^3, losing the Gaussian characteristics due to the cloud masking algorithm. The number of in situ IWC measurements from CEPEX, CRYSTAL-FACE, and NAMMA campaigns is indicated after the acronym.

Table 3. The *Ze*-IWC Relations Proposed From Various Studies

94-GHz *Ze*-IWC Relations	$\log_{10}(a)$	b	Comments[a]
Atlas et al. [1995]	−1.19	0.58	Midlatitude: FIRE-I
Brown et al. [1995]	−0.82	0.74	Low and midlatitudes: CEPEX (−10°C to −65°C), EUCREX (−10°C to −50°C)
Aydin and Tang [1997]	−0.98	0.48	Model study
Liu and Illingworth [2000]	−0.86	0.64	Low and midlatitudes: CEPEX (−10°C to −65°C), EUCREX (−10°C to −50°C)
Sassen et al. [2002]	−0.92	0.70	Midlatitudes and high latitudes: ground Cloud heights: −25°C to −40°C
Heymsfield et al. [2005]	−0.17	0.64	Subtropics: CRYSTAL-FACE Cloud heights: −25°C to −52°C $Ze < 0.0032$ $0.0032 < Ze < 3.97$ $Ze > 3.97$
	−0.71	0.42	
	−0.65	0.52	
Hogan et al. [2006]	$-00189T - 1.19$	0.85	Midlatitude, EUCREX (−10°C to −50°C)
Protat et al. [2007]	$-00002T - 0.61$	$0.97 + 0.0046T$	Low and midlatitudes: CLARE98, CARL99, ARM, EUCREX, FASTEX, CEPEX and CRYSTAL-FACE
Sayres et al. [2008]	−0.89	0.70	Subtropics: CRYSTAL-FACE Cloud heights: 15–17 km

[a]*Ze* is radar reflectivity factor in mm^6/m^3 and *T* is air temperature in °C.

maintain approximately the same log-linear slope, or pdf $\sim Ze^{-1}$, at altitudes above 12 km where cloud occurrence frequency drops exponentially with height. The *Ze* pdf slope turns shallower, or pdf $\sim Ze^{-0.9}$, at altitudes <12 km, and reveals moderate saturation at $Ze > 10$ dBZ and severe saturation at $Ze > 15$ dBZ, as expected for Mie scattering effects at 94 GHz.

[35] The IWC retrievals from CloudSat *Ze* can differ considerably from each other depending on the method used. Figures 5b–5d compare the R04, H06, and S08 IWC retrievals with aircraft measurements from CEPEX, CRYSTAL-FACE and NAMMA campaigns at 8, 10, and 12 km. The pdf's from the three CloudSat IWC retrievals agree well (within a factor of 2) for IWC between 10 and 500 mg/m^3 but show significant differences at high IWC values. Nevertheless, none of these algorithms is developed for very high IWC values. Overall, the R04 retrieval is closer to S08 at these altitudes, both low against H06. Because of the log-linear *Ze*-IWC relation used by H06 and S08, the *Ze*-to-IWC conversion also distorts the Gaussian distribution. Note that the R04 IWC pdf flattens at IWC $< \sim 1$ mg/m^3, indicative of incomplete noise statistics. At IWC > 500 mg/m^3, pdf differences among three CloudSat retrievals may be resulted from the microphysical assumptions made by these methods. The higher retrieved IWC from H06, as noted in H06, could be due to its ice density model, which is inappropriate for the applications involving large ice particles. *Heymsfield et al.* [2008] also compared radar IWCs retrieved from various methods, and found that the H06 method would produce a higher retrieval at large IWCs for temperatures between −20°C and −50°C but the difference is smaller at temperatures <−60°C. *Eriksson et al.* [2008] also evaluated CloudSat R04 and R03 retrievals and compared them to those from *Liu and Illingworth* [2000] and from a method using the MH97 size distribution. They found that the retrieval from *Liu and Illingworth* [2000] agrees well with the MH97 method, showing a pdf between those from the R03 and R04 retrievals.

[36] To validate the pdf slope in the upper troposphere, we compare the pdf's of in situ IWC measurements with CloudSat IWC in Figures 5b–5d. The pdf slope reflects nature of cloud inhomogeneity and variability of atmospheric dynamics. Because airborne campaigns were often designed to go after cloudy atmospheres, the observed cloud occurrence frequency may be higher than global statistics as observed by CloudSat. As shown in Figure 5, the CloudSat pdf slopes agree reasonably well with CEPEX at 12 km and with the CRYSTAL-FACE statistics at all three altitudes. The pdf slopes of the in situ data show large differences at 8 and 10 km, likely due to sampling biases intended by these campaigns.

5. Cloud Ice Comparisons

5.1. Spatial Averaging

[37] Comparing cloud ice measurements is challenging because of large cloud inhomogeneity and variability. As a bulk quantity, the IWC and IWP measurements represent a spatial average of cloud ensembles. Since the measurement volume can vary from instrument to instrument, as a result, the observed IWC or IWP statistics may differ, depending on degree of cloud inhomogeneity. As shown in Figure 2, MLS IWC measurements correspond to a tangential volume over $\sim 300 \times 7 \times 4$ km^3, whereas a CloudSat measurement has a volume of $\sim 1.8 \times 1.4 \times 0.5$ km^3 in the along-track, cross-track and vertical dimensions. For fair comparisons we need to take into account effects from volume averaging associated with each technique. In the comparisons associated with data from different measurement volumes, we choose to average the data set with finer spatial resolution to match the measurement volume of lower resolution. For example, in CloudSat-MLS comparison the along-track averaging ($\sim 300 \times 4$ km^2) by MLS dominates the smearing effect, and we average ~5000 CloudSat measurements in this domain since CloudSat profiles are separated by ~1 km in distance with 0.25 km. The cross-track averaging is neglected in this study.

[38] Effects of spatial averaging on cloud ice statistics is difficult to evaluate without knowing the true cloud variability. Prior to the launch of CloudSat, information on IWC inhomogeneity is very limited. In situ measurements from aircraft campaigns have very few long-leg flights, and the samplings are often biased toward certain cloud types (e.g., cirrus and outflow anvils). Therefore, instead of evaluating averaging effects on MLS measurements, we compare MLS and CloudSat measurements directly by averaging CloudSat data to match MLS measurement volume.

5.2. Cloud Versus Precipitation Ice

[39] Remotely-sensed IWC or IWP are different from the quantity produced by numerical models, and observation-model comparisons must be interpreted with caution in terms of cloud and precipitation ice. Most of the observing

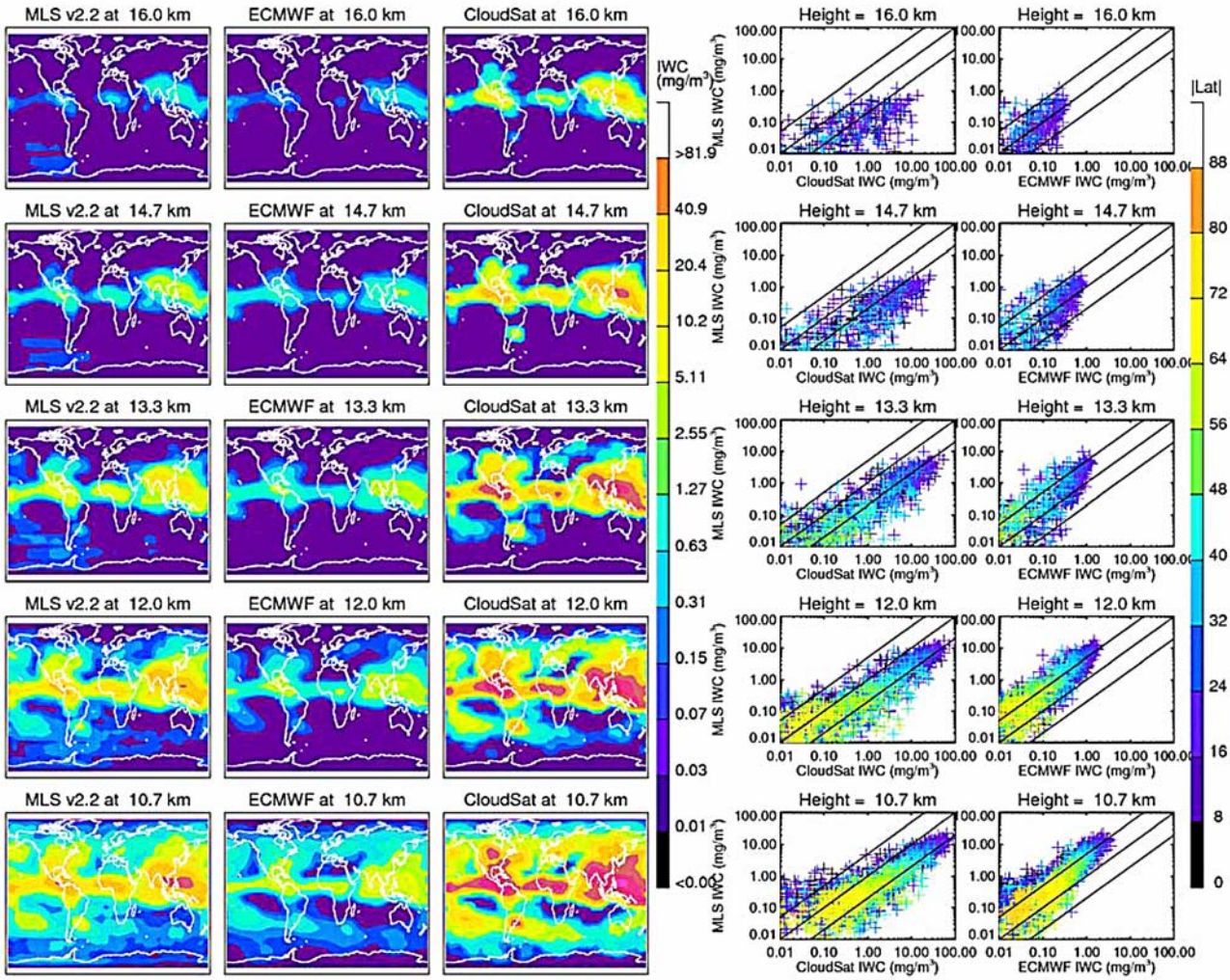

Figure 6. MLS, European Center for Medium range Weather Forecasting (ECMWF), and CloudSat and IWC maps for 7 July to 16 August 2006 at pressure altitudes of 10.7, 12, 13.3, 14.7, and 16 km. The maps have the same color scale on a 4° × 8° Lat-Lon grid, and a 3-point smoothing is applied to the grid box averages. The striping distribution in MLS IWC maps at middle and high southern latitudes is an artifact of false detection. The ECMWF and CloudSat IWC data are averaged vertically to match the MLS vertical resolution (~4 km) at these altitudes. On the right are scatter plots of the IWC values from the maps, where colors denote latitudes from the equator and lines of the 1:1, 1:5, and 5:1 ratios are shown.

techniques based on ice particle scattering cannot distinguish between cloud and precipitation ice. The precipitation ice (i.e., snowflakes, graupels) is often associated with large ice crystals and a substantial falling speed. Scattering effects from cloud and precipitation ice particles are usually mixed together to produce reflectivity in the active case or T_{cir} in the passive case. Therefore, the remotely sensed IWC is often a combination of cloud and precipitation ice. On the other hand, cloud and precipitation ice are usually treated differently in the numerical models. The prognostic product from ECMWF and GEOS-5.1 analyses is for cloud ice, and ice mass from snow and precipitation must be derived differently [*Waliser et al.*, 2009].

5.3. IWC Comparisons

[40] Figure 6 shows the IWC maps from MLS, ECMWF and CloudSat averaged at pressure altitudes of 10.7, 12, 13.3, 14.7, and 16 km for 7 July to 16 August 2006. The IWC morphology is consistent among the three data sets, showing similar enhancements in the Asian and American monsoon regions. CloudSat mean IWC is generally 3–5 times greater than MLS ones, but both are greater than the ECMWF mean. Some of the MLS clouds at Southern Hemispheric high latitudes, showing latitude strips, are artifacts from false detection with the V2.2 algorithm [*Wu et al.*, 2008]. The V2.2 cloud detection threshold is generally improved over V1.5 but false detection remains large at high latitudes and affects the IWC average if it is <0.15 mg/m^3. The enhancement over southern Argentina at 10.7, 12, and 13.3 km is captured by MLS, CloudSat, and ECMWF but the ECMWF amplitude is much weaker than the observations and CloudSat can even see it at 14.7 and 16 km. In the Northern Hemisphere MLS cloud ice distribution is overall consistent with CloudSat at 10.7–16 km, but CloudSat values are higher, which cause partly a wider (northward) spread of IWC distribution at 13.3–16 km.

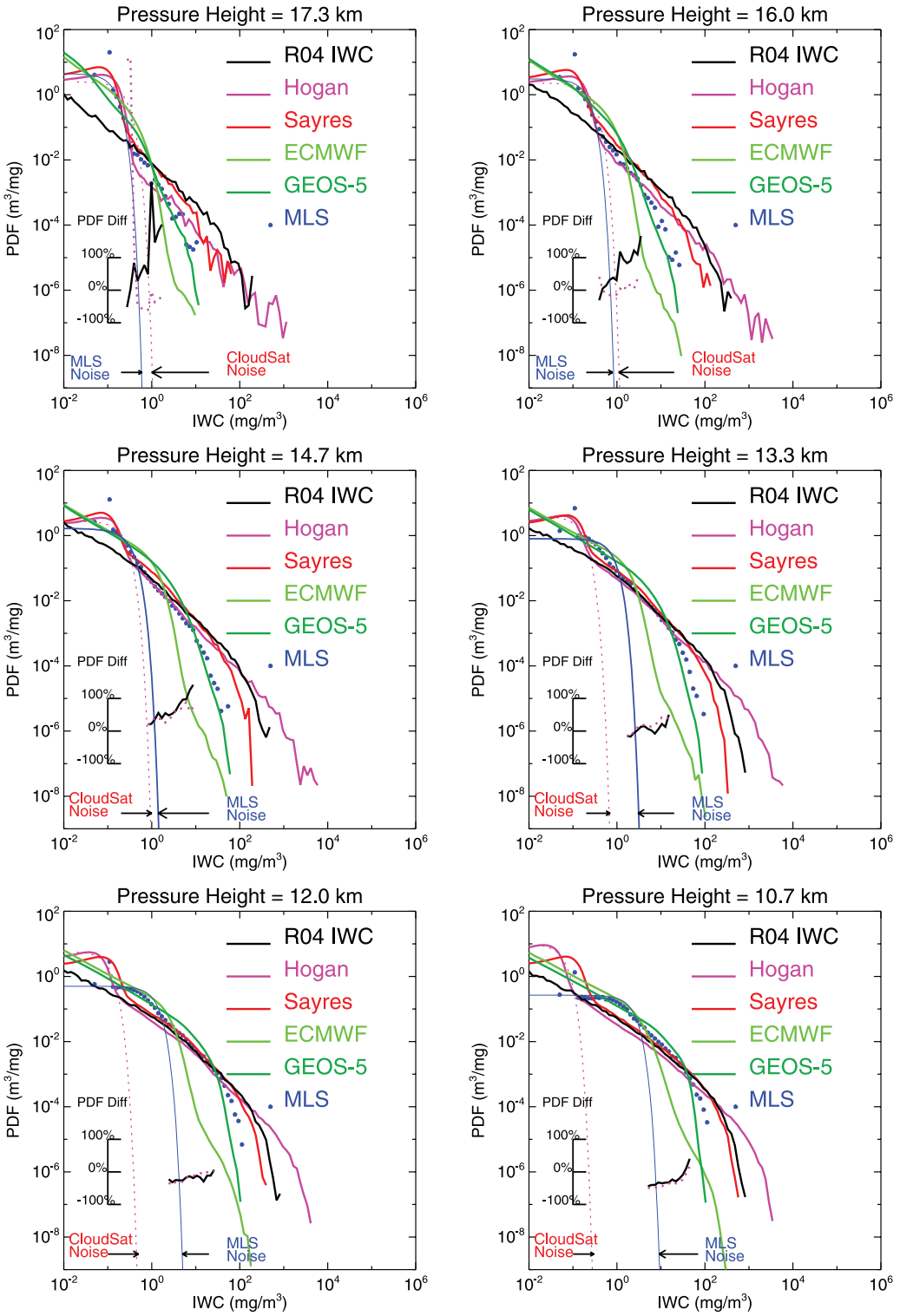

Figure 7. The pdf's of ECMWF, GEOS-5, MLS, and CloudSat IWC for 7 July to 16 August 2006 in a tropical bin of 25°S–25°N. Seven pressure levels at 261, 215, 177, 147, 121, 100, and 83 hPa, which correspond to nominal altitudes of 10.7, 12, 13.3, 14.7, 16, and 17.3 km, respectively, are presented. Three CloudSat retrievals (R04, H06, and S08), are shown to highlight large differences at IWC > ~30 mg/m^3. The IWC retrievals from H06 and S08 start to deviate at IWC > ~100 mg/m^3. Rising pdf's at small IWC values are manifestations of the measurement noise, and the fitted Gaussian curves are shown with the estimated CloudSat (H06) and MLS Gaussian noise indicated. The short curves in the lower part of each panel with scale on the left are the pdf percentage difference between CloudSat (R04 and H06) and MLS IWC. Only the percentage differences in the overlapped sensitivity range are shown, which is defined as (CloudSat − MLS)/CloudSat × 100 and labeled inside each panel.

[41] The monthly mean ECMWF IWCs at 10.7–16 km are generally lower compared to MLS and CloudSat by a factor of ~5 and ~20, respectively. In addition, ECMWF lacks midlatitude cloud ice at 10.7–13.3 km altitudes, although the model captures the feature over the southern Argentina. The H06 and S08 IWC retrievals (not shown) have a mean and distribution similar to the R04 retrieval. *Li et al.* [2005] compared MLS January IWC observations to an earlier version of ECMWF analysis made on a 1° × 1° resolution. The morphologies of MLS and ECMWF IWC in the upper troposphere appear to agree well, but MLS is generally higher by a factor of 2–3 over tropical landmasses, which is similar to the differences found here. In a follow-on study for the entire 2005, *Li et al.* [2007] found that the model lacks convective activity at pressures >147 hPa and cannot maintain the initial cloud ice mass at 147 hPa for more than 24 h. These studies raised an important point about comparing satellite observations with modeled IWC, which has to do with how cloud and precipitation ice are treated by models and how they are measured by satellite sensors. More detailed discussions on this issue can be found in the work of *Waliser et al.* [2009] in this issue. On the other hand, the high IWC values and differences in the observations do raise a concern about the assumptions made in the retrievals, in particular, the assumption about ice particle size distribution. Uncertainties about ice microphysics, as recognized by *Wu et al.* [2008] and *Austin et al.* [2009], can have a very large impact on accuracy of the retrieved IWC. Nevertheless, comparisons between radar and in situ data suggested that IWC uncertainty from various CloudSat algorithms is likely within a factor of 2–3.

[42] The grid box average in IWC maps does not give the proper evaluation for measurement differences among various sensors because sensitivity differences are neglected. An alternative approach is to characterize measurement uncertainties through the normalized pdf whereby the IWC difference is a function of IWC value (Appendix A). Figure 7 shows comparisons of the pdf's of MLS, CloudSat and ECMWF IWCs at altitudes of 10.7–17.3 km where the CloudSat and ECMWF data have been averaged horizontally and vertically to match the MLS measurement volume (see Figure 2). The data used in Figure 7 are restricted to the tropical region (25°S–25°N), which embrace most of the cloud ice in the upper troposphere. For the H06 and S08 IWC retrievals, the measurement noise can be estimated from the rising pdf at small IWC values. The estimated precisions in Figure 7 correspond to an averaged IWC over the MLS measurement volume (~300 × 7 × 4 km^3). Similarly, the ECMWF and GEOS-5.1 IWCs are compared to MLS observations by averaging model IWC to match the MLS measurement volume.

[43] The measurement noise, relative bias, and sensitivity range of MLS, CloudSat, ECMWF and GEOS-5.1 data sets are reflected in Figure 7. The measurement noise of MLS, H06 and S08 retrievals, which are estimated from the pdf at small values, show that MLS has a slightly better precision at 16 and 17.3 km, but worse at lower altitudes. The R04 retrieval does not have such information because of the noise truncation. MLS sensitivity also degrades for large IWC values due to saturation by thick-and-dense clouds [*Wu et al.*, 2008]. This degradation in MLS sensitivity reflects fewer large IWC measurements, causing a steep drop in the pdf tail. CloudSat sensitivity to IWC, on the other hand, has a wider dynamic range because of better cloud penetration ability with the radar. As discussed above, the R04 IWC pdf is overall more consistent to S08, but both are lower than H06 at large IWC values.

[44] In the overlapped sensitivity range (approximately 1–50 mg/m^3), the MLS and CloudSat IWC agree reasonably well at these altitudes, showing the pdf differences less than 50%. The MLS-CloudSat differences exhibit somewhat larger differences at 16 and 17.3 km, where MLS has its best sensitivity, with MLS being lower against CloudSat R04 IWC. The differences appear to increase with IWC in the overlapped sensitivity range. In a comparison to R03 data, the MLS-CloudSat difference was found to be much smaller at these altitudes [*Wu et al.*, 2008]. Nonetheless, the agreement between MLS and R04 IWC pdf is encouraging overall, given that the MLS retrieval is limited by saturation in sensitivity at altitudes <14.7 km. At altitudes >14 km, however, the large differences between MLS and CloudSat R04 retrievals warrants further investigation.

[45] ECMWF IWC, although showing global distributions similar to MLS and CloudSat in Figure 6 exhibits quite different pdf's in Figure 7. The pdf's of ECMWF IWC are generally biased high (by a factor of 5–8) at small (<5 mg/m^3) IWCs but low at large (>5 mg/m^3) IWCs. At all altitudes, the ECMWF pdf's drop off too sharply at large IWCs but manages to maintain the roughly same slope at small IWCs. In other words, cloud occurrence frequency appears too high for small cloud ice values but too low for large ice values. The sharp dropoff at large IWCs could be a manifestation of the cloud ice removal/precipitation processes in the model. As discussed in the beginning of this section, ECMWF IWC contains only cloud ice and excludes snow or precipitation contributions, whereas the satellite observations include all hydrometeors in the air.

[46] Like ECMWF IWC, GEOS-5.1 IWC has a high bias at small IWCs but a low bias at large IWCs. The pdf of GEOS-5.1 IWC agrees better with the observations at the large IWC end. Nonetheless, a drop in the GEOS-5.1 pdf appears similar to ECMWF at the large IWC. The largest differences between GEOS-5.1 and ECMWF IWCs are found in the range of 5–50 mg/m^3 where the GEOS-5.1 pdf tends to drop off gradually. For the monthly mean IWC (not shown), GEOS-5.1 values are slightly higher than MLS but still lower than CloudSat R04 retrievals.

[47] Cloud inhomogeneity can contribute to some of the pdf differences in the observed IWCs. In small IWC cases, MLS can penetrate most of the clouds in the path to measure average IWC in the path volume. In this case, different cloud distributions from inhomogeneity in the measurement path have small effects on the relation between IWC and cloud-induced radiance [*Davis et al.*, 2007]. *Wu et al.* [2008] estimated cloud inhomogeneity effects on the MLS IWC retrieval using inhomogeneous IWC distributions as observed by CloudSat, and found that cloud inhomogeneity tended to produce a random error of ~100% in the retrieval and a scaling error of 40–70% for IWC < 50 mg/m^3. However, cloud inhomogeneity becomes important for large IWC cases where MLS has difficulty to penetrate all the clouds in the path. In this case, cloud fraction and horizontal/vertical wave spectra of IWC will interact

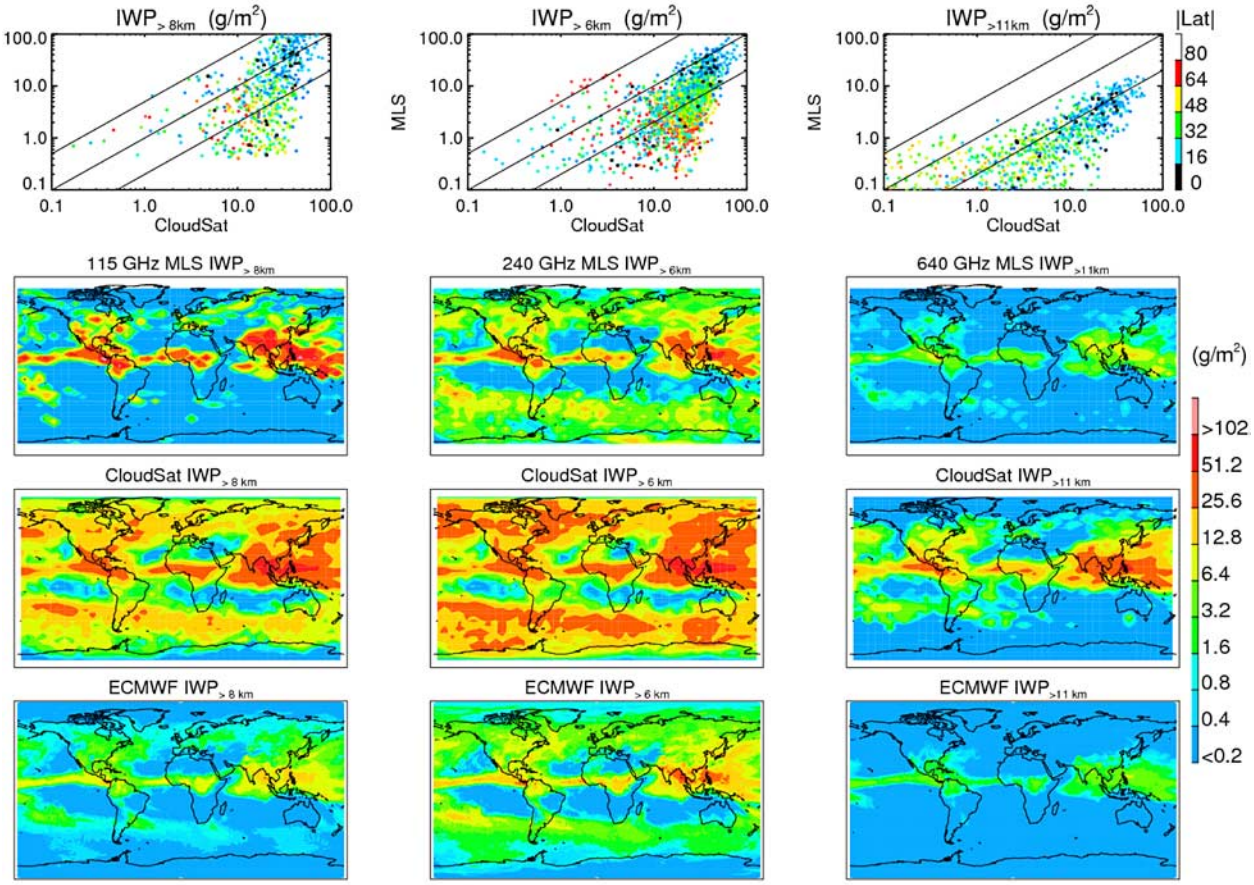

Figure 8. MLS, CloudSat, and ECMWF IWP maps (4° × 8° latitude-longitude grid) for 7 July to 16 August 2006. The three partial columns, $IWP_{>8km}$, $IWP_{>6km}$, and $IWP_{>11km}$, are based on MLS 115, 240, and 640 GHz measurements. All IWP maps share the same color scale on the right, and a 3-point smoothing is applied to the averages. Correlation between MLS and CloudSat grid box averages is shown in the top row with latitude in colors, and the 1:1, 1:5, and 5:1 ratios are shown to guide comparisons.

with clear-sky emissions through radiative transfer along the path, producing a nonlinear or saturated relation between IWC and cloud-induced radiance. In the case of saturation, the retrieved MLS IWC does not reflect the true average over the measurement volume, which leads to a substantial drop in IWC pdf. Because CloudSat can still penetrate these clouds, this pdf drop with MLS IWC manifests itself as the increasing deviation from the pdf of CloudSat IWC. For example, this large deviation starts to occur for IWC > ~50 mg/m^3 at 14.7 km.

5.4. IWP Comparisons

[48] Comparing IWP measurements from different passive sensors can be more difficult than doing IWC because of additional uncertainties associated with the IWP retrievals, such as the bottom height of IWP measurements. IWP measurements are often a partial column, or pIWP, in which cloud self-extinction and attenuation from water vapor and liquid water prevents radiation from interacting with all clouds in the path. However, these problems are largely mitigated with active microwave techniques. Therefore, in this study CloudSat IWP data are generally treated as the truth to understand and evaluate sensitivity of pIWP retrievals with passive sensors, including MLS 115, 240, and 640 GHz measurements. Passive techniques have advantage of providing a 2-D distribution of cloud ice over a wide swath.

[49] Because the penetration depth of passive sensors can vary largely with water vapor loading and cloud self-extinction in the atmosphere, a retrieved pIWP has the bottom height varying with tropospheric water vapor amount and pIWP amount itself. In the low-tangent-height limb-viewing case, the column bottom for MLS 115, 240, and 640 GHz window channels are at ~8, ~6, and ~11 km on average. For fair IWP comparisons, we integrate CloudSat IWC for the similar columns as defined by MLS 115, 240, and 640 GHz, and compare monthly averages and pdf's of these pIWPs. Similarly, we carry out the pIWP comparisons for the matched volume among MLS, ECMWF and GEOS-5.1.

[50] In the case of precipitating and mixing-phase clouds, a problem for both passive and active microwave techniques, attenuation by liquid clouds in the lower troposphere can reduce the IWP sensitivity with passive techniques. Uncertainties of IWP measurements tend to be larger in mixed-phase clouds (e.g., in polar regions), where temperatures are near or warmer than −40°C [*Hogan et al.*, 2003].

[51] As shown in Figure 8, MLS, CloudSat, and ECMWF pIWPs exhibit similar geographical distributions for the

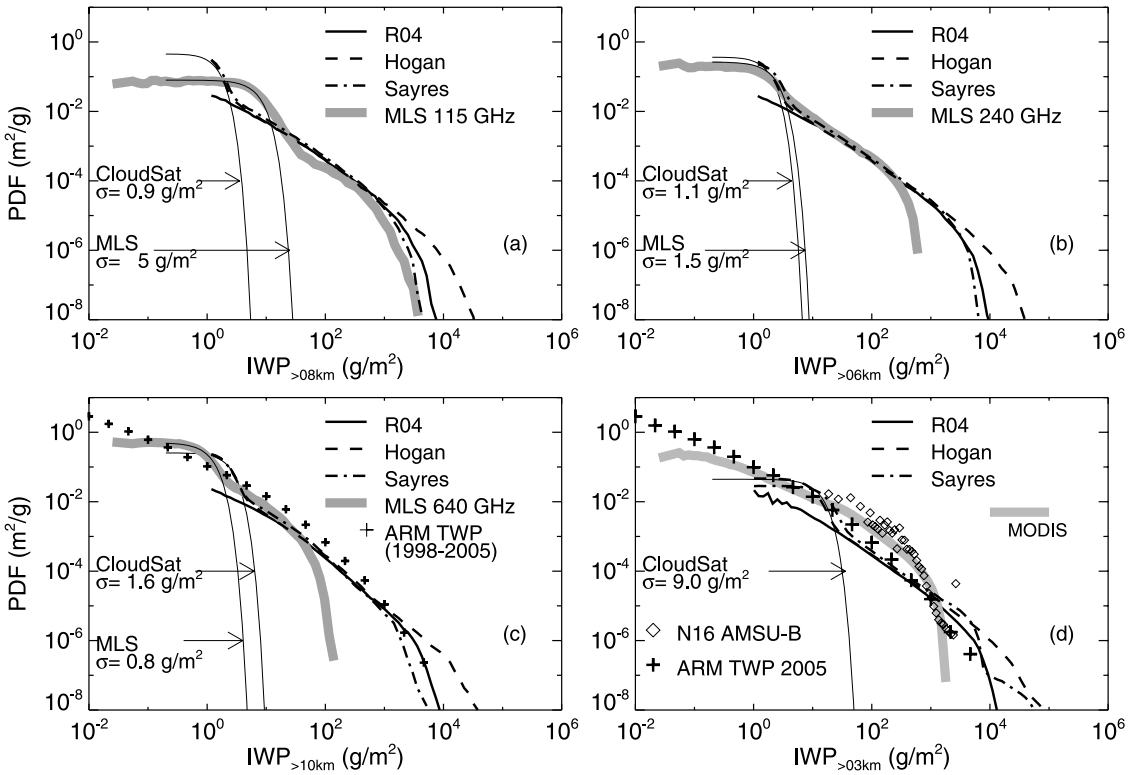

Figure 9. (a–c) The pdf's of the tropical (25°S–25°N) IWPs from CloudSat R04, H06, S08, and MLS for 7 July to 16 August 2006. The three partial IWPs correspond to MLS measurements from three different frequencies. To match CloudSat IWP to MLS measurement volume, we also average the CloudSat data horizontally with a running window of approximately 124, 61, and 29 km for comparison with MLS 115, 240, and 640 GHz observations, respectively. The rising pdf at small IWP values is fitted with a Gaussian function with σ = 5, 0.8, and 1.5 g/m^2 for CloudSat and σ = 52, 4.2, and 0.1 g/m^2 for MLS. (d) The pdf's of Advanced Microwave Sounding Unit-B (AMSU-B), Atmospheric Radiation Measurement Program Tropical West Pacific (ARM TWP), and CloudSat IWPs. Except for AMSU-B, all IWPs in this panel are a partial column above 3 km, or $IWP_{>3km}$. No spatial averaging is applied to CloudSat data, and a Gaussian function with σ = 9 g/m^2 is fitted to the CloudSat H06 retrieval. The pdf of ARM TWP $IWP_{>3km}$ from 1998–2005 is also included in Figure 9c, and all the ARM data are from 3-h averaged measurements.

three partial columns as defined by MLS 115, 240, and 640 GHz channels. However, there are some significant differences. Lack of cloud ice in MLS 115-GHz map at midlatitudes and high latitudes is worth noting because of the similar penetration depths between MLS 115 and 240 GHz pIWP. Since these clouds are evident in the 240-GHz map, the missing midlatitude clouds may suggest poorer sensitivity of the 115 GHz channel to smaller ice particles. On the other hand, lack of the 640-GHz cloud ice at midlatitudes and high latitudes is indicative of the limited penetration depth with the 640 GHz channel. Even though the 640-GHz channel has better sensitivity to cloud scattering than 240 GHz, it cannot reach the midtroposphere to see the clouds there. Compared to the observations, the ECMWF pIWPs are generally lower, which may explain lack of ECMWF cloud ice above 8 km over the northern Africa and the Rockies. Furthermore, the ECMWF $IWP_{>11km}$ misses most of the cloud ice at midlatitudes and high latitudes, and the cloud ice over the SPCZ is weak compared to the observations.

[52] The corresponding grid box pIWP averages from MLS and CloudSat are scattered widely and deviated from the 1:1 line (Figure 8, top). In the $IWP_{>8km}$ case, MLS 115 GHz measurements are slightly higher at large $IWP_{>8km}$ values but lower for small values. The MLS retrievals with a high bias are located mostly at low latitudes, and in these cases the 115 GHz $IWP_{>8km}$ retrievals are often higher than the 240 GHz $IWP_{>6km}$ retrievals. The inconsistency among MLS retrievals is likely due to uncertainty about the estimated bottom height of these pIWPs. In the thick cloud cases, strong cloud extinction can raise the bottom height higher than 6 km at 240 GHz, but not as much as at 115 GHz. In other words, the 115 GHz channel is less sensitive to cloud extinction than a channel at 240 GHz. Thus, the 240 GHz pIWP should be interpreted as a column from a higher altitude than 6 km in thick cloud cases. The correlation between MLS 240 GHz and CloudSat $IWP_{>6km}$ generally falls between the 1:1 and 1:5 lines with MLS being lower. A low (by ~5×) MLS bias is also evident in the $IWP_{>11km}$ scatter plot, of which the differences has a similar order of magnitude to MLS and CloudSat IWC differences at high altitudes.

[53] The scattered relations between MLS and CloudSat pIWPs in Figure 8 can be partly attributed to differences in measurement sensitivity, which are revealed in the pdf

comparison. Figures 9a–9c compare the pdf's of MLS and CloudSat pIWPs from a tropical (25°S–25°N) band during the period 7 July to 16 August 2006. There is a dip at ~50 g/m^2 in Figure 9a, and MLS IWP$_{>8km}$ is overall lower than CloudSat for values greater than ~50 g/m^2. In Figure 9a, the pdf's from H06, S07 and R04 retrievals agree well for IWP$_{>8km}$ < 10^3 g/m^2, but deviate from each other at larger values with R04 and S07 being closer together. In the 115 GHz case, there is a broad sensitivity overlap (20–3000 g/m^2) between MLS and CloudSat IWP$_{>8km}$, where MLS agrees generally well with CloudSat R04 and S08 retrievals.

[54] From the pdf's in Figure 9b, we estimate the precisions of MLS 240-GHz and CloudSat IWP$_{>6km}$ retrievals, and they are comparable (1.1 and 1.5 g/m^2, respectively). Both retrievals agree well in the overlapped sensitivity range (5–300 g/m^2). The sharp dropoff in the MLS pdf at IWP$_{>6km}$ > 300 g/m^2 suggests saturation in MLS sensitivity. In the saturation cases MLS can still detect clouds but may underestimate the IWP$_{>6km}$ value. The CloudSat R04 and S08 retrievals in the IWP$_{>6km}$ case agree well with each other, both showing a dropping pdf tail below the H06 one at IWP$_{>6km}$ > 1000 g/m^2.

[55] MLS 640-GHz IWP$_{>11km}$ overlaps with CloudSat in sensitivity over a narrow (5–100 g/m^2) range (Figure 9c). The R04 pdf at IWP$_{>11km}$ < ~5 g/m^2 starts to be questionable because it is dominated by noise and can be affected by truncated statistics in the R04 IWC retrieval. Although MLS IWP$_{>11km}$ shows a slightly better (0.8 g/m^2) precision than CloudSat, it becomes saturated at ~100 g/m^2. Compared to the pdf of ARM TWP IWP$_{>11km}$, CloudSat and MLS results exhibit a similar pdf slope but with a lower cloud occurrence frequency. Again, the different CloudSat retrievals agree well for small IWP$_{>11km}$ values but deviate from each other at IWP$_{>11km}$ > 1000 g/m^2.

[56] In Figure 9d, the CloudSat IWP$_{>3km}$ is compared with MODIS, AMSU-B, and ARM TWP observations. The CloudSat IWP$_{>3km}$ is integrated up from 3 km below which there is very little contribution. The estimated precision for CloudSat IWP$_{>3km}$ is ~9 g/m^2, and the three CloudSat retrievals show a consistent pdf up to ~ 5000 g/m^2. Between 10 and 5000 g/m^2, the ARM pdf agree relatively well with CloudSat except for a steeper slope at IWP$_{>3km}$ > 100 g/m^2. The ARM data are higher at small IWP$_{>3km}$ values and lower at large IWP$_{>3km}$ values. As in MLS 115-GHz case, the AMSU-B retrieval lacks sensitivity to mid- and high-latitude cloud ice (not shown). Both MODIS and AMSU-B IWPs are higher (by a factor of 5–8) compared to CloudSat in the range between 10 and 1000 g/m^2 but drop off sharply at IWP > 500 g/m^2 because of sensitivity losses. It is interesting to observe that both passive IR and microwave techniques reveal a similar sensitivity loss at large pIWP values, which could be explained by the dependence of their cloud detection on the vertical temperature gradient in the troposphere. The temperature gradient provides a similar dynamic range for IR and microwave cloud detections [*Berg et al.*, 1999]. The AMSU-B retrieval (from 89–150 GHz) is expected to have a pdf dropoff similar to the MLS 115 and 240 GHz retrievals because of the similar frequencies. The large CloudSat-AMSU-B difference is unlikely caused by their different measurement areas: CloudSat (1.1 km by 1.8 km) versus AMUS-B footprints (15 km diameter). Including the effect of this spatial average will lower the CloudSat pdf by ~10%, which makes the CloudSat-AMSU-B difference even greater. To reconcile the observed differences, one must reexamine the assumptions made on cloud microphysics in these retrievals.

6. Conclusions and Future Work

[57] We have compared statistical properties and global morphology of IWC and pIWP measurements from Aura MLS, CloudSat, and correlative data sets. Measurement noise, relative bias and sensitivity of these cloud ice observations are characterized and discussed. The typical precision value of MLS IWC, which is an average over a ~300 × 7 × 4 km^3 volume, varies between 0.06 and 1 mg/m^3 at 83 and 215 hPa with sensitivity saturated at ~100 mg/m^3. The MLS pIWPs derived from 115, 240 and 640 GHz measurements, which represent an areal average on 120 × 12, 60 × 6, and 30 × 3 km^2 footprints respectively, are a partial column with the bottom height at approximately 8, 6, and 11 km. The typical precision for these pIWPs are 5, 1.5, and 0.8 g/m^2 with sensitivity saturated at about 2000, 500, and 100 g/m^2, respectively.

[58] Statistical properties of CloudSat reflectivity are studied in terms of the normalized pdf, and the estimated precision of cloud reflectivity is −31 dBZ, or ~3 dBZ better than the design specification. In this study we compared three CloudSat IWC retrievals: R04 2B-IWC-RO, *Hogan et al.* [2006] (or H06), and *Sayres et al.* [2008] (or S08). In the upper troposphere (> ~8 km), all the retrievals show similar pdf distributions at IWC between 10 and 500 mg/m^3, and the agreement between R04 and S08 extends to ~2000 mg/m^3. At the large IWCs, the R04 and S08 retrievals are significantly lower than H06. For IWC < ~500 mg/m^3, the three CloudSat retrievals have a pdf slope generally consistent with in situ observations (particularly good agreement with CRYSTAL-FACE). The estimated single-profile precision of CloudSat IWC measurements varies from 0.4 mg/m^3 at 8 km to 1.6 mg/m^3 at 12 km. The R04 IWC retrieval is significantly improved over R03 in handling large-IWC cases, but the R04 retrieval is overall larger than R03. The estimated single-profile precision for the R04 IWP$_{>3km}$ is ~9 g/m^2.

[59] We compared MLS and CloudSat cloud ice measurements with other correlative data, and the main findings from this study are summarized as follows:

[60] 1. MLS V2.2 and CloudSat R04 retrievals show consistent IWC morphologies on monthly maps but the R04 IWC grid box averages are generally higher by a factor of ~5. Much of the difference is due to MLS sensitivity degradation at large IWC values. The MLS and CloudSat retrievals agree reasonably well in IWC pdf, showing differences less than 50% in the overlapped sensitivity range. At 15–17 km the R04 retrievals are high against MLS and the difference increases rapidly with IWC. At these altitudes, MLS IWC has its best precision and usually is not limited by sensitivity degradation. Comparisons between MLS and R03 [*Wu et al.*, 2008], on the other hand, show rather small differences.

[61] 2. ECMWF IWC grid box averages are lower compared to MLS V2.2 and CloudSat R04 retrievals by a factor

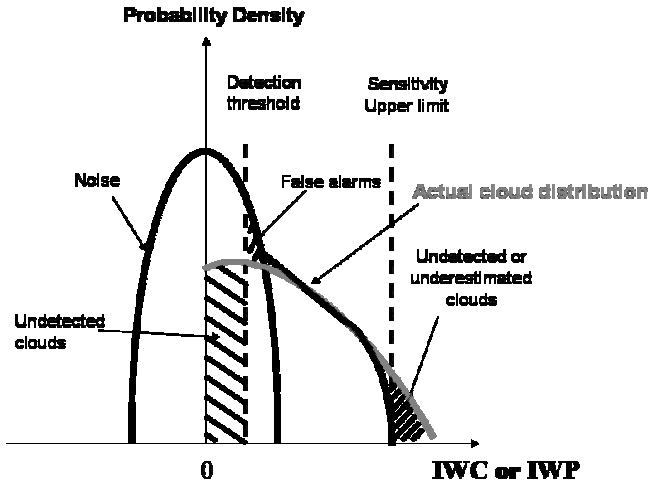

Figure A1. A schematic diagram to illustrate different portions of a measured cloud pdf. The gray curve is the true pdf from a cloud ice ensemble that is only measured partially by a sensor (solid black) because of measurement noise and sensitivity limitation. Depending on the threshold used for cloud detection, false cloud detection and missing clouds are unavoidable and can become a problem to compare cloud occurrence frequency from different sensors. Directly comparing the normalized pdf's from different sensors can identify measurement noise, sensitivity range, and accuracy in a cloud ice data set.

of ~5 and ~20, respectively. The differences between ECMWF IWC and the observations vary with IWC, showing that the model results are higher at small IWCs but lower at large IWCs. The ECMWF pdf appears to drop off too sharply at large IWC values. The differences between modeled and observed IWC need to be reconciled in terms of cloud and precipitation ice because they are treated differently in the model whereas observing techniques usually cannot distinguish between the two [*Waliser et al.*, 2009]. Similar model-observation differences are found in the pdf comparisons of GEOS-5.1, MLS and CloudSat IWCs.

[62] 3. The pIWPs from MLS 115, 240 and 640 GHz (or $IWP_{>8km}$, $IWP_{>6km}$, and $IWP_{>11km}$, respectively) produce consistent monthly morphologies with those derived from CloudSat IWC. Lack of midlatitude and high-latitude cloud ice in the 115-GHz $IWP_{>8km}$ map is likely due to poor sensitivity at this frequency, but lack of midlatitude clouds in the $IWP_{>11km}$ map is mostly due to the inability of penetrating into the midtroposphere at 640 GHz. Compared to CloudSat, MLS 115-GHz $IWP_{>8km}$ is slightly higher at large values but lower at small values whereas MLS 640-GHz $IWP_{>11km}$ retrieval is lower by a factor of 5. The 240-GHz $IWP_{>6km}$ retrieval has the best agreement with CloudSat, showing a slightly low bias at small IWP values. All ECMWF pIWPs have a low bias compared to the observations, consistent with the low bias found in the IWC comparisons.

[63] 4. The AMSU-B and MODIS IWPs show respectively ~5× and ~8× high biases against CloudSat in between IWP between 10 and 500 g/m^2. The high biases are most likely due to assumptions on cloud microphysics in the AMSU-B and MODIS retrievals. Both AMSU-B and MODIS sensitivities start to decay at pIWP > 500 g/m^2 because of saturation.

[64] We have learned from this study that the dynamic range of cloud ice variability is so large that no single instrument can measure all. Individual techniques are often limited by measurement noise at small IWC values and sensitivity degradation at large values. With the launch of CloudSat and CALIPSO, cloud remote sensing has entered into a new era. These active sensors greatly extend the cloud sensitivities we had from passive sensor like MLS, AMSU-B and MODIS instruments. The passive sensors will likely remain as the key technique in the future to map 2D and 3D distributions of cloud ice but require the active sensors to calibrate their measurements. Hence, joint analyses of the A-Train active-passive cloud data have an important implication for future cloud remote sensing, particularly in reducing uncertainties of cloud ice observations associated with cloud microphysics and with passive techniques. For example, intercomparisons of radiative transfer modeling for collocated cloud measurements will lead to additional constraints on the cloud microphysics assumptions used in the retrievals. To better understand cloud and precipitation ice, the 13.8-GHz Tropical Rainfall Measuring Mission Precipitation Radar (TRMM PR) data (1998 to present) can extend sensitivity to precipitation ice, which will be a valuable data source to constrain microphysical properties of large hydrometeors. Together, these instruments now provide sensitivity needed to cover the entire dynamic range of cloud and precipitation ice, and the satellite observations begin to show appreciable precision and accuracy for climate models to probe the cloud feedback problem in the Earth's climate system.

Appendix A: Normalized Probability Density Function

[65] The probability density function (pdf) analysis provides great insights to statistical properties of a data set and can be used to compare these properties among data sets without imposing strict collocation-and-coincidence requirements. Particularly for cloud comparisons, the collocation-and-coincidence requirements are sometimes too

difficult to meet, which leave with too few samples to draw any statisitically significant conclusion. A pdf should be normalized such that the area under the distribution is unity in order to compare with one from another data set. Comparing cloud observations in form of normalized pdf requires no cloud detection threshold, which can be problematic in the cases where sensors have different sensitivities. Cloud occurrence frequency and fraction are among the quantities of this kind, and they are sensor-dependent, calibration-dependent, and platform-dependent. As shown in Figure A1, the normalized pdf preserves several important statistical properties of a data set, such as measurement noise, bias, and sensitivity.

[66] If data statistics are fully preserved, the measurement noise will show up as a Gaussian function at small values. In a log-log coordinate, the noise manifest itself as a rising curve at small values with a plateau at the top of the normalized pdf. Usually, the noise pdf is symmetric about zero but can be skewed in the presence of a bias, which can be verified with the pdf of negative IWC or IWP values. The normalized pdf can be used to evaluate the level of confidence in cloud detection, which apparently depends on cloud occurrence frequency (COF). As shown in Figure 5a, a high COF normally raises the cloud pdf, and different thresholds should be used for cloud detection depending on the expected COF. False alarm and missing clouds can be determined in the case where a threshold is used for separating clear versus cloudy skies (Figure A1). In comparing different pdf's, a bias or scaling error would appear as distorted or shifted pdf's relative to each other. Degradation in sensitivity due to saturation to large IWC or IWP will result in a dropoff in pdf at the end of large values.

[67] The pdf method has disadvantages in distinguishing or characterizing cloud property changes due to other causes. One of the disadvantages with the pdf method is lack of information on spatial distribution and inhomogeneity. For example, one can have the same pdf, which is from a mixture of regions A and B, to a mixture of regions C and D. This example involves four ensembles which can be quite different but AB is similar to CD. Another disadvantage is that pdf can sometimes hide differences among various retrieval algorithms since it only provides gross statistics of the retrieval results.

[68] **Acknowledgments.** This work was performed at the Jet Propulsion Laboratory, California Institute of Technology, under contract with the National Aeronautics and Space Administration (NASA). We thank our MLS and CloudSat colleagues for successful instrument operation and data processing. For this study, we especially thank Gerald Mace, Robin Hogan, and Alain Protat for valuable discussions on radar algorithms. We also thank ECMWF for providing their analyses data to the AIRS team at JPL for carrying out this study. Efforts from Cooperative Institute for Research in the Atmosphere (CIRA) for making AMSU-B data available and helpful comments from three anonymous reviewers are also acknowledged.

References

Atlas, D., S. Y. Matrosov, A. J. Heymsfield, M.-D. Chou, and D. B. Wolf (1995), Radar and radiation properties of ice clouds, *J. Appl. Meteorol.*, *34*, 2329–2345, doi:10.1175/1520-0450(1995)034<2329:RARPOI>2.0.CO;2.

Austin, R. T., and G. L. Stephens (2001), Retrieval of stratus cloud microphysical parameters using millimeter-wave radar and visible optical depth in preparation for CloudSat: 1. Algorithm formulation, *J. Geophys. Res.*, *106*, 28,233–28,242, doi:10.1029/2000JD000293.

Austin, R. T., A. J. Heymsfield, and G. L. Stephens (2009), Retrieval of ice cloud microphysical parameters using the CloudSat millimeter-wave radar and temperature, *J. Geophys. Res.*, *114*, D00A23, doi:10.1029/2008JD010049.

Aydin, K., and C. X. Tang (1997), Relationships between IWC and polarimetric radar measurands at 94 and 220 GHz for hexagonal columns and plates, *J. Atmos. Oceanic Technol.*, *14*, 1055–1063, doi:10.1175/1520-0426(1997)014<1055:RBIAPR>2.0.CO;2.

Barnes, W. L., T. S. Pagano, and V. V. Salomonson (1998), Prelaunch characteristics of the Moderate Resolution Imaging Spectroradiometer (MODIS) on EOS-AM1, *IEEE Trans. Geosci. Remote Sens.*, *36*, 1088–1100, doi:10.1109/36.700993.

Bauer, P., G. Kelly, and E. Andersson (2002), SSM/I radiance assimilation at ECMWF. Proceedings of the ECMWF/GEWEX workshop on "Humidity Analysis", Eur. Cent. for Medium-Range Weather Forecasts, Reading, 8–11 July.

Benedetti, A., G. L. Stephens, and J. M. Haynes (2003), Ice cloud microphysics retrievals from millimeter radar and visible optical depth using an estimation theory approach, *J. Geophys. Res.*, *108*(D11), 4335, doi:10.1029/2002JD002693.

Berg, W., J. J. Bates, and D. L. Jackson (1999), Analysis of upper-tropospheric water vapor brightness temperatures from SSM/T2, HIRS, and GMS-5 VISSR, *J. Appl. Meteorol.*, *38*, 580–595, doi:10.1175/1520-0450(1999)038<0580:AOUTWV>2.0.CO;2.

Bloom, S. C., et al. (2005), The Goddard Earth Observing Data Assimilation System, GEOS DAS Version 4.0.3: Documentation and Validation, *Tech. Rep. 104606 V26*, 166 pp., NASA, Washington, D. C.

Brown, P. R. A., et al. (1995), The role of spaceborne millimeter-wave radar in the global monitoring of ice cloud, *J. Appl. Meteorol.*, *34*, 2346–2366, doi:10.1175/1520-0450(1995)034<2346:TROSMW>2.0.CO;2.

Chevallier, F., P. Lopez, A. M. Tompkins, M. Janisková, and E. Moreau (2004), The capability of 4D-Var systems to assimilate cloud-affected satellite infrared radiances, *Q. J. R. Meteorol. Soc.*, *130*, 917–932, doi:10.1256/qj.03.113.

Clothiaux, E. E., et al. (2000), Objective determination of cloud heights and radar reflectivities using a combination of active remote sensors at the ARM CART sites, *J. Appl. Meteorol.*, *39*, 645–665, doi:10.1175/1520-0450(2000)039<0645:ODOCHA>2.0.CO;2.

Clothiaux, E. E., et al. (2001), *The ARM Millimeter Wave Cloud Radars (MMCRs) and the Active Remote Sensing of Clouds (ARSCL) Value Added Product (VAP)*, *DOE Tech. Memo. ARM VAP-002.1*, 56 pp., U. S. Dept. of Energy, Washington, D. C.

Davis, C. P., H. C. Pumphrey, K. F. Evans, S. Buehler, and D. L. Wu (2007), 3D polarised simulations of space-borne passive mm/sub-mm midlatitude cirrus observations: A case study, *Atmos. Chem. Phys.*, *7*, 4149–4158.

Deng, M., and G. G. Mace (2006), Cirrus microphysical properties and air motion statistics using cloud radar Doppler moments. Part I: Algorithm description, *J. Appl. Meteorol.*, *45*(12), 1690–1709, doi:10.1175/JAM2433.1.

Eriksson, P., M. Ekstrom, B. Rydberg, and D. P. Murtagh (2007), First Odin sub-mm retrievals in the tropical upper troposphere: Ice cloud properties, *Atmos. Chem. Phys.*, *7*, 471–483.

Eriksson, P., et al. (2008), Comparison between first Odin-SMR, Aura MLS and CloudSat retrievals of cloud ice masses in the upper tropical troposphere, *Atmos. Chem. Phys.*, *8*, 1937–1948.

Evans, K. F., et al. (1998), Modeling of submillimeter passive remote sensing of cirrus clouds, *J. Appl. Meteorol.*, *37*, 184–205, doi:10.1175/1520-0450(1998)037<0184:MOSPRS>2.0.CO;2.

Gill, A. E. (1980), Some simple solutions for heat-induced tropical circulation, *Q. J. R. Meteorol. Soc.*, *106*, 447–462, doi:10.1002/qj.49710644905.

Halpern, D., and C. W. Hung (2001), Satellite observations of the southeast Pacific intertropical convergence zone during 1993–1998, *J. Geophys. Res.*, *106*, 28,107–28,112, doi:10.1029/2000JD000056.

Hartmann, D. L., and K. Larson (2002), An important constraint on tropical cloud-climate feedback, *Geophys. Res. Lett.*, *29*(20), 1951, doi:10.1029/2002GL015835.

Heymsfield, A. J., and L. J. Donner (1990), A scheme for parameterizing ice-cloud water content in general circulation models, *J. Atmos. Sci.*, *47*, 1865–1877.

Heymsfield, A. J., and G. M. McFarquhar (1996), On the high albedos of anvil cirrus in the tropical Pacific warm pool: Microphysical interpretations from CEPEX, *J. Atmos. Sci.*, *53*, 2424–2451, doi:10.1175/1520-0469(1996)053<2424:HAOCIT>2.0.CO;2.

Heymsfield, A. J., and C. M. R. Platt (1984), A parameterization of the particle size spectrum of ice clouds in terms of the ambient temperature and the ice water content, *J. Atmos. Sci.*, *41*, 846–855.

Heymsfield, A. J., Z. Wang, and S. Matrosov (2005), Improved radar ice water content retrieval algorithms using coincident microphysical and radar measurements, *J. Appl. Meteorol.*, *44*, 1391–1412, doi:10.1175/JAM2282.1.

Heymsfield, A. J., et al. (2008), Testing IWC retrieval methods using radar and ancillary measurements with in-situ data, *J. Appl. Met. Clim.*, *47*, 135–163, doi:10.1175/2007JAMC1606.1.

Hogan, R. J., et al. (2003), Characteristics of mixed-phase clouds. I: Lidar, radar and aircraft observations from CLARE'98, *Q. J. R. Meteorol. Soc., Part A*, *129*(592), 2089–2116.

Hogan, R. J., M. P. Mittermaier, and A. J. Illingworth (2006), The retrieval of ice water content from radar reflectivity factor and temperature and its use in evaluating a mesoscale model, *J. Appl. Meteorol.*, *45*, 301–317, doi:10.1175/JAM2340.1.

Hong, G., G. Heygster, J. Miao, and K. Kunzi (2005), Detection of tropical deep convective clouds from AMSU-B water vapor channels measurements, *J. Geophys. Res.*, *110*, D05205, doi:10.1029/2004JD004949.

Houghton, J. T., Y. Ding, and M. Noguer (2001), *Climate Change 2001: The Scientific Basis*, 881 pp., Cambridge Univ. Press.

Houze, R. A., Jr., S. S. Chen, D. E. Kingsmill, Y. Serra, and S. E. Yuter (2000), Convection over the Pacific Warm Pool in relation to the atmospheric Kelvin-Rossby wave, *J. Atmos. Sci.*, *57*, 3058–3089, doi:10.1175/1520-0469(2000)057<3058:COTPWP>2.0.CO;2.

Im, E., S. L. Durden, and C. Wu (2005), Cloud profiling radar for the CloudSat mission, *IEEE Aerosp. Electron. Syst. Mag.*, *20*, 15–18, doi:10.1109/MAES.2005.1581095.

Intrieri, J. M., G. L. Stephens, W. L. Eberhard, and T. Uttal (1993), A method for determining cirrus cloud particle sizes using lidar and radar backscatter technique, *J. Appl. Meteorol.*, *32*(6), 1074–1082, doi:10.1175/1520-0450(1993)032<1074:AMFDCC>2.0.CO;2.

Jarnot, R. F., V. S. Perun, and M. J. Schwartz (2006), Radiometric and spectral performance and calibration of the GHz bands of EOS MLS, *IEEE Trans. Geosci. Remote Sens.*, *44*(5), 1131–1143, doi:10.1109/TGRS.2005.863714.

Li, J.-L., et al. (2005), Comparisons of EOS MLS cloud ice measurements with ECMWF analyses and GCM simulations: Initial results, *Geophys. Res. Lett.*, *32*, L18710, doi:10.1029/2005GL023788.

Li, J.-L., J. H. Jiang, D. E. Waliser, and A. M. Tompkins (2007), Assessing consistency between EOS MLS and ECMWF analyzed and forecast estimates of cloud ice, *Geophys. Res. Lett.*, *34*, L08701, doi:10.1029/2006GL029022.

Li, L., and S. L. Durden (2006), *Level 1 B CPR Process Description and Interface Control Document*, *JPL Doc. D-20308*, Jet Propul. Lab., Pasadena, Calif.

Lietzke, C. E., C. Deser, and H. Thomas (2001), Vonder Haar: Evolutionary structure of the eastern Pacific double ITCZ based on satellite moisture profile retrievals, *J. Clim.*, *14*, 743–751, doi:10.1175/1520-0442(2001)014<0743:ESOTEP>2.0.CO;2.

Liu, C., and A. J. Illingworth (2000), Toward more accurate retrievals of ice water content from radar measurements of clouds, *J. Appl. Meteorol.*, *39*, 1130–1146, doi:10.1175/1520-0450(2000)039<1130:TMAROI>2.0.CO;2.

Liu, W. T., and X. Xie (2002), Double intertropical convergence zones—A new look using scatterometer, *Geophys. Res. Lett.*, *29*(22), 2072, doi:10.1029/2002GL015431.

Mace, G. G., E. E. Clothiaux, and T. P. Ackerman (2001), The composite characteristics of cirrus clouds: Bulk properties revealed by one year of continuous cloud radar data, *J. Clim.*, *14*, 2185–2203, doi:10.1175/1520-0442(2001)014<2185:TCCOCC>2.0.CO;2.

Mace, G. G., R. Marchand, and G. L. Stephens (2007), Global hydrometeor occurrence as observed by CloudSat: Initial observations from summer 2006, *Geophys. Res. Lett.*, *34*, L09808, doi:10.1029/2006GL029017.

Matrosov, S. Y., A. V. Korolev, and A. J. Heymsfield (2002), Profiling cloud mass and particle characteristic size from Doppler radar measurements, *J. Atmos. Oceanic Technol.*, *19*, 1003–1018, doi:10.1175/1520-0426(2002)019<1003:PCIMAP>2.0.CO;2.

McFarquhar, G. M., and A. J. Heymsfield (1996), Microphysical characteristics of three anvils sampled during the central equatorial pacific experiment, *J. Atmos. Sci.*, *53*, 2401–2423, doi:10.1175/1520-0469(1996)053<2401:MCOTAS>2.0.CO;2.

McFarquhar, G. M., and A. J. Heymsfield (1997), Parameterization of tropical cirrus ice crystal size distributions and implications for radiative transfer: Results from CEPEX, *J. Atmos. Sci.*, *54*, 2187–2200, doi:10.1175/1520-0469(1997)054<2187:POTCIC>2.0.CO;2.

Protat, A., J. Delanoe, D. Bouniol, A. J. Heymsfield, A. Bansemer, and P. Brown (2007), Evaluation of ice water content retrievals from cloud radar reflectivity and temperature using a large airborne in-situ microphysical database, *J. Appl. Meteorol. Climatol.*, *46*, 557–572, doi:10.1175/JAM2488.1.

Ramanathan, V., et al. (1989), Cloud-radiative forcing and climate: Results from the Earth radiation budget experiment, *Science*, *243*, 57–63, doi:10.1126/science.243.4887.57.

Randall, D. A., et al. (2007), Climate models and their evaluation, in *Climate Change 2007: The Physical Sciences Basis*, *Contribution of Working Group I to the Fourth Assessment Report of the Intergovernmental Panel on Climate Change*, edited by S. Solomon et al., chap. 8, pp. 589–662, Cambridge Univ. Press, U. K.

Salomonson, V. V., W. L. Barnes, P. W. Maymon, H. E. Montgomery, and H. Ostrow (1989), MODIS: advanced facility instrument for studies of the Earth as a system, *IEEE Trans. Geosci. Remote Sens.*, *27*, 145–153, doi:10.1109/36.20292.

Sassen, K., Z. Wang, V. I. Khvorostyanov, G. L. Stephens, and A. Bennedetti (2002), Cirrus cloud ice water content radar algorithm evaluation using an explicit cloud microphysical model, *J. Appl. Meteorol.*, *41*, 620–628, doi:10.1175/1520-0450(2002)041<0620:CCIWCR>2.0.CO;2.

Sayres, D. S., J. B. Smith, J. V. Pittman, E. M. Weinstock, J. G. Anderson, G. Heymsfield, L. Li, A. M. Fridlind, and A. S. Ackerman (2008), Validation and determination of ice water content radar reflectivity relationships during CRYSTAL-FACE: Flight requirements for future comparisons, *J. Geophys. Res.*, *113*, D05208, doi:10.1029/2007JD008847.

Schwartz, M. J., et al. (2008), Characterization of MJO-related upper tropospheric hydrological processes using MLS, *Geophys. Res. Lett.*, *35*, L08812, doi:10.1029/2008GL033675.

Stephens, G. L. (1978), Radiation profiles in extended water clouds: II. Parameterizations schemes, *J. Atmos. Sci.*, *35*, 2123–2132, doi:10.1175/1520-0469(1978)035<2123:RPIEWC>2.0.CO;2.

Stephens, G. L. (2005), Cloud feedbacks in the climate system: A critical review, *J. Clim.*, *18*, 237–273, doi:10.1175/JCLI-3243.1.

Stephens, G. L., and C. D. Kummerow (2007), The remote sensing of clouds and precipitation from space: A review, *J. Atmos. Sci.*, *64*, 3742–3765, doi:10.1175/2006JAS2375.1.

Stephens, G. L., et al. (2002), The CloudSat mission and the EOS constellation: A new dimension of space-based observations of clouds and precipitation, *Bull. Am. Meteorol. Soc.*, *83*, 1771–1790, doi:10.1175/BAMS-83-12-1771.

Tanelli, S., L. Durden, E. Im, K. S. Pak, D. G. Reinke, P. Partain, J. M. Haynes, and R. T. Marchand (2008), CloudSat's cloud profiling radar after two years in orbit: Performance, calibration, and processing, *IEEE Trans. Geosci. Remote Sens.*, *46*, 3560–3573.

Waliser, D. E., and C. Gautier (1993), A satellite-derived climatology of the ITCZ, *J. Clim.*, *6*, 2162–2174, doi:10.1175/1520-0442(1993)006<2162:ASDCOT>2.0.CO;2.

Waliser, D. E., et al. (2009), Cloud ice: A climate model challenge with signs and expectations of progress, *J. Geophys. Res.*, *114*, D00A21, doi:10.1029/2008JD010015.

Waters, J. W., et al. (2006), The Earth observing system microwave limb sounder (EOS MLS) on the Aura satellite, *IEEE Trans. Geosci. Remote Sens.*, *44*(5), 1075–1092, doi:10.1109/TGRS.2006.873771.

Weng, F., and N. C. Grody (2000), Retrieval of ice cloud parameters using a microwave imaging radiometer, *J. Atmos. Sci.*, *57*, 1069–1081, doi:10.1175/1520-0469(2000)057<1069:ROICPU>2.0.CO;2.

Wu, D. L., W. G. Read, A. E. Dessler, S. C. Sherwood, and J. H. Jiang (2005), UARS MLS cloud ice measurements and implications for H2O transport near the tropopause, *J. Atmos. Sci.*, *62*(2), 518–530, doi:10.1175/JAS-3382.1.

Wu, D. L., J. H. Jiang, and C. P. Davis (2006), EOS MLS cloud ice measurements and cloudy-sky radiative transfer model, *IEEE Trans. Geosci. Remote Sens.*, *44*(5), 1156–1165, doi:10.1109/TGRS.2006.869994.

Wu, D. L., et al. (2008), Validation of aura Microwave Limb Sounder (MLS) IWC measurement, *J. Geophys. Res.*, *113*, D15S10, doi:10.1029/2007JD008931.

Zhao, L., and F. Weng (2002), Retrieval of ice cloud parameters using the Advanced Microwave Sounding unit, *J. Appl. Meteorol.*, *41*, 384–395, doi:10.1175/1520-0450(2002)041<0384:ROICPU>2.0.CO;2.

R. T. Austin and G. L. Stephens, Department of Atmospheric Science, Colorado State University, Fort Collins, CO 80523, USA.

M. Deng, Department of Atmospheric Science, University of Wyoming, Laramie, WY 82071, USA.

S. L. Durden, J. H. Jiang, A. Lambert, J.-L. Li, N. J. Livesey, S. Tanelli, D. G. Vane, D. E. Waliser and D. L. Wu, Jet Propulsion Laboratory, California Institute of Technology, Pasadena, CA 91109, USA. (dong.l.wu.@jpl.nasa.gov)

A. J. Heymsfield, National Center for Atmospheric Research, Boulder, CO 80307, USA.

G. M. McFarquhar, Department of Atmospheric Sciences, University of Illinois at Urbana-Champaign, Urbana, IL 61820, USA.

J. V. Pittman, NASA Marshall Space Flight Center, Huntsville, AL 35812, USA.